What Drives the Intensification of Mesoscale Convective Systems over the West African Sahel under Climate Change?

RORY G. J. FITZPATRICK,[a,e] DOUGLAS J. PARKER,[a] JOHN H. MARSHAM,[a] DAVID P. ROWELL,[b] FRANCOISE M. GUICHARD,[c] CHRIS M. TAYLOR,[d] KERRY H. COOK,[e] EDWARD K. VIZY,[e] LAWRENCE S. JACKSON,[a] DECLAN FINNEY,[a] JULIA CROOK,[a] RACHEL STRATTON,[b] AND SIMON TUCKER[b]

[a] *Institute for Climate and Atmospheric Sciences, University of Leeds, Leeds, United Kingdom*
[b] *Met Office, Exeter, United Kingdom*
[c] *Centre National de Recherches Météorologiques, Toulouse, France*
[d] *Centre for Ecology and Hydrology, Wallingford, United Kingdom*
[e] *Jackson School of Geosciences, The University of Texas at Austin, Austin, Texas*

(Manuscript received 28 May 2019, in final form 2 January 2020)

ABSTRACT

Extreme rainfall is expected to increase under climate change, carrying potential socioeconomic risks. However, the magnitude of increase is uncertain. Over recent decades, extreme storms over the West African Sahel have increased in frequency, with increased vertical wind shear shown to be a cause. Drier midlevels, stronger cold pools, and increased storm organization have also been observed. Global models do not capture the potential effects of lower- to midtropospheric wind shear or cold pools on storm organization since they parameterize convection. Here we use the first convection-permitting simulations of African climate change to understand how changes in thermodynamics and storm dynamics affect future extreme Sahelian rainfall. The model, which simulates warming associated with representative concentration pathway 8.5 (RCP8.5) until the end of the twenty-first century, projects a 28% increase of the extreme rain rate of MCSs. The Sahel moisture change on average follows Clausius–Clapeyron scaling, but has regional heterogeneity. Rain rates scale with the product of time-of-storm total column water (TCW) and in-storm vertical velocity. Additionally, prestorm wind shear and convective available potential energy both modulate in-storm vertical velocity. Although wind shear affects cloud-top temperatures within our model, it has no direct correlation with precipitation rates. In our model, projected future increase in TCW is the primary explanation for increased rain rates. Finally, although colder cold pools are modeled in the future climate, we see no significant change in near-surface winds, highlighting avenues for future research on convection-permitting modeling of storm dynamics.

1. Introduction

The socioeconomic risks to vulnerable people across West Africa due to climate change are manifold (USAID 2017). Of particular interest are projections of the frequency and intensity of extreme precipitation events. Mesoscale convective systems (MCSs) are responsible for the majority of annual rainfall over the Sahel (Laurent et al. 1998; Laing et al. 1999; Fink and Reiner 2003); understanding future change of these events is pivotal to ascertaining future risk associated to rainfall.

The purpose of this study is to understand the processes by which climate change can affect MCS precipitation rates, particularly the 99th percentile of surface precipitation rates from MCSs (hereafter termed the extreme precipitation rate), over the West African Sahel. We use a state-of-the-art regional climate model without any active convection parameterization scheme to understand how variability on the synoptic-to-climate time scale may affect MCS extreme precipitation rates.

Denotes content that is immediately available upon publication as open access.

Supplemental information related to this paper is available at the Journals Online website: https://doi.org/10.1175/JCLI-D-19-0380.s1.

Corresponding author: Rory Fitzpatrick, r.g.j.fitzpatrick@austin.utexas.edu

DOI: 10.1175/JCLI-D-19-0380.1

The multidecadal drought afflicting the Sahel in the 1970s and 1980s has been followed by a so-called "recovery period" (Nicholson 2005; Hagos and Cook 2008; Lebel and Ali 2009; Lodoun et al. 2013; Evan et al. 2015; Sanogo et al. 2015) during which average annual rainfall has returned to near-long-term mean levels (Lélé and Lamb 2010, their Fig. 1). However, the nature of intraseasonal rainfall variability has changed over the Sahel during recent decades, with an observed increase in the frequency of very rainy MCSs separated by longer periods of little to no rainfall (Panthou et al. 2014; Taylor et al. 2017). More intense rain events carry increased risk of flooding, with observational studies suggesting that flood events over the Sahel have become more frequent over the past decades (Panthou et al. 2014; Nka et al. 2015; Panthou et al. 2018; Tazan et al. 2019; Wilcox et al. 2018). Intense but temporarily sparse rain events can also deteriorate soil quality through nutrient runoff (Panagos et al. 2017).

Taylor et al. (2017) observe a threefold increase in the frequency of early-evening MCSs with mean cloud-top temperature <-75°C over the Sahel since the 1980s. This increase is associated with an intensification of midday wind shear in the vertical pressure column, henceforth wind shear, calculated as the difference between low-level southwesterly/westerly winds and midlevel easterly winds, as well as a drying of the Saharan air layer. Cold pools and organized squall lines have also been observed to intensify over the same time frame, although the presence of drier midlevel air and stronger cold pools may be coincidental and not dynamically linked (cf. James and Markowski 2010).

On the storm time scale, Taylor et al. (2017) found that ambient wind shear intensity is significantly correlated with the mean cloud-top temperature of MCSs, with subsequent observational work suggesting that ambient wind shear strength may also influence the maximum precipitation rates of storms (Fig. S1 in the online supplemental material). These findings are consistent with previous studies highlighting the role of wind shear in organizing convection (Browning and Ludlam 1962; Moncrieff 1978, 1981; Thorpe et al. 1982; Dudhia et al. 1987; Nicholls et al. 1988; Rotunno et al. 1988; Mapes 1993; Houze 1993; Tao et al. 1995; Ferrier et al. 1996; LeMone et al. 1998; Mohr and Thorncroft 2006; Alfaro 2017).

Cloud-resolving model (CRM) studies have suggested that other ambient and storm-relative variables are more important than wind shear in controlling MCS precipitation rates. Takemi (2007, 2010, 2014) found that the vertical distribution of high CAPE in the lower troposphere controls mean MCS precipitation rates to a greater extent than lower/midtropospheric shear. However, Takemi (2010) also found an inverse relationship between lower-tropospheric temperature lapse rate and the maximum precipitation intensity of MCSs (their Fig. 14b), implying that increased CAPE could be negatively correlated with maximum precipitation rates. A similar result is found in Lucas et al. (2000), where enhanced wind shear positively impacts total precipitation from MCSs, but negatively impacts maximum precipitation rates. These results imply that storm-related drivers can be shown to positively or negatively impact MCS intensity depending on the definition of storm intensity. It is for this reason we primarily focus on extreme precipitation rates.

Finally, variability in moisture and ascent rates within MCSs have previously been identified as influential in MCS precipitation rate variability. Increased inflow of moist, buoyant air, and vertical ascent within convective updrafts increase maximum precipitation rates (Alfaro 2017), as does enhanced lower-tropospheric relative humidity (Lucas et al. 2000). Takemi (2014) hypothesized that increased precipitable water available to a developing MCS will be positively correlated with maximum precipitation rates. This theory is not explicitly tested by the author.

Rising temperatures under global warming have the potential to intensify many of the MCS intensity drivers discussed above. Amplified warming of the Sahara (Cook and Vizy 2015; Vizy and Cook 2017) will increase the meridional temperature gradient across West Africa, leading to enhanced lower- to midtropospheric wind shear over the Sahel, in part through the enhancement of the African easterly jet (Cook 1999). It is posited that a greater future meridional temperature gradient over West Africa will lead to heavier precipitating MCSs under climate change due to the strong water vapor feedback over the region (Dong and Sutton 2015; Evan et al. 2015). Through the Clausius–Clapeyron relationship, it is expected that increased warming over the Sahel will lead to an increase in total column water (TCW); this relationship has been identified previously within the model used in this study (Kendon et al. 2019). Over the tropics, Takemi (2012) and Takemi et al. (2012) also find an increase in lower-tropospheric CAPE under global warming. In our analysis, we examine the magnitude by which the above-identified MCS intensity drivers increase in a potential future climate, and their subsequent dynamic effect on MCS precipitation rates.

Coarse-resolution models with convection parameterization schemes, which do not account for the role of wind shear, can struggle to model Sahelian storms and their intensities accurately (Marsham et al. 2013). Convection-permitting models at ~4 km horizontal

resolution have been shown to realistically simulate present day monsoon flow, cold pool outflows (Marsham et al. 2013), convergence (Birch et al. 2014a,b), the diurnal cycle of rainfall (Vizy and Cook 2018, 2019), and agricultural decision-maker relevant monsoon metrics (Garcia-Carreras et al. 2015). Future climate simulations of the West African climate at convection-permitting resolutions therefore provide an opportunity to better understand changes in MCS dynamics under global warming.

Section 2 describes the model used in this paper, with section 3 explaining the methods employed. Sections 4–7 provide results: first, we identify climatological changes in the West African monsoon between the current and future Convection Permitting for Africa (CP4-A) climate runs, then we analyze future changes in distributions of MCS precipitation intensity relative to the current climate and the potential causes at different times of the day. Section 8 gives conclusions and recommendations for future work.

2. Data

Within the Future Climate for Africa (FCFA) program, the Improving Model Processes for African Climate (IMPALA) project has produced two 10-yr model simulations for the African continent at the convection-permitting horizontal grid spacing of ~4.4 km. These simulations are referred to hereafter CP4-A (Stratton et al. 2018; Kendon et al. 2019). The CP4-A simulations project the changes in African climate for the end of the twenty-first century with ~4 K sea surface temperature (SST) warming and ~5 K mean near-surface temperature increase over the continent (Kendon et al. 2019). The model has 80 vertical levels with finer vertical resolution within the tropopause and boundary layer. We provide a brief overview of the model and its quality below.

CP4-A is a regional model spanning longitudes 24°W–56°E, and latitudes 45°S–39°N. The model is forced by lateral boundary conditions from an atmosphere-only version of the Met Office global climate model (GCM) with ~25 km horizontal grid spacing, and with prescribed daily SSTs. Land surface properties are initialized using the most recent JULES land surface scheme (Walters et al. 2019), and allowed to evolve freely over time. CP4-A uses an applied moisture conservation scheme (Aranami et al. 2015) and a three-dimensional blended boundary layer scheme (Boutle et al. 2014). The large-scale cloud scheme is described in Smith (1990), and has been used in other convection-permitting versions of the Met Office Unified Model. The cloud scheme diagnoses liquid cloud fraction and condensed water when the grid-box mean relative humidity exceeds a critical value. Ice water content is determined by the microphysics scheme, with cloud fractions then diagnosed as in Abel et al. (2017). Other parameterization schemes are documented in Stratton et al. (2018, their Table 2). Both CP4-A, and the driving GCM, use the Even Newer Dynamics for General Atmospheric Modeling of the Environment (ENDGame) dynamical core (Wood et al. 2014). The ENDGame dynamical core has been shown previously to improve the representation of key processes over West Africa, particularly the seasonal progression of monsoon rains (Vellinga et al. 2016; Fitzpatrick 2016, appendix B).

In each climate respectively, the same SSTs are prescribed for the driving GCM, CP4-A, and the parameterized model. Current climate SSTs are provided from the Reynolds daily observational dataset (Reynolds et al. 2007). Future climate SSTs are calculated first by quantifying the climatological change in SST values simulated between 1975–2005 and 2085–2115 from a GCM run using phase 5 of the Coupled Model Intercomparison Project (CMIP5) representative concentration pathway 8.5 (RCP8.5). This climatological SST change was calculated monthly, interpolated both spatially and temporally, and added to the current climate values to produce future SSTs. Greenhouse gases are taken from the RCP8.5 scenario for 2100; however the same ozone and aerosol climatology is used in both simulations. Future changes in precipitation rates across West Africa between the two simulations can be attributed to rising temperatures and increases in greenhouse gases.

CP4-A has no convection scheme of any kind, using just model dynamics to explicitly represent convective clouds. We note the caveat that a model at 4.4 km grid spacing with no convective parameterization scheme may not capture the complexity of convective development simulated in higher resolution CRM studies, as model resolution has been highlighted in the past as a key issue in correctly simulating cloud processes (e.g., Lin et al. 2012). With that said, the decision to have no active convection scheme allows for a clearer comparison between convection permitting and parameterized models produced during IMPALA.

Kendon et al. (2019) find that CP4-A better recreates observed high precipitation rates over Africa compared to the parameterized-convection counterpart model and projects a larger future increase in intense precipitation rates (their Fig. 1). Berthou et al. (2019b) find that CP4-A accurately simulates the frequency of MCSs over the AMMA-CATCH observational sites. Stratton et al. (2018) and Berthou et al. (2019b) also show that the seasonal transition of monsoon rains across West Africa

is better captured in CP4-A compared to its parameterized convection counterpart, as well as a reduction of the persistent dry bias within CP4-A. However, Crook et al. (2019) highlight that CP4-A fails to simulate MCSs of comparable area to the largest ones observed, or speeds comparable to the quickest systems.

Simulations at the temporal and spatial scale of CP4-A incur an extensive computational expense. As such, there has been a need for compromise with regards to model design and output. There exists only one model representation for the current and future climates respectively. The authors stress that the findings of this paper are based on a research model, with a particular set of boundary conditions from one global model, and so cannot be taken as projections with a certainty level attached, but rather as results from climate sensitivity study.

The authors also stress that the two 10-yr simulations are not considered as historical and future climatologies. Decadal and multidecadal variability of ambient conditions across West Africa can influence our results. We explore the role of this variability further in section 6a.

3. Methods

In this paper, we analyze the climatic drivers of changes in early-evening MCS extreme precipitation rates (the 99th percentile of MCS precipitation rate) over the Sahel. The calculation methods for extreme precipitation rate and other considered MCS-relevant metrics are presented in Table 1. We define the Sahel as 10°–18°N, 15°W–15°E (displayed in Fig. 3); the suitability of this region for both climates is explored in section 4. The codes employed in this paper are available at http://doi.org/10.5281/zenodo.2560371 and http://doi.org/10.5281/zenodo.2560410.

MCSs are classified as any contiguous structure with an area of cold-cloud [outgoing longwave radiation (OLR) $\leq 167\,\mathrm{W\,m^{-2}}$] of at least $25\,000\,\mathrm{km^2}$ simulated during July–September. Extreme precipitation rates are therefore calculated across a region of at least $250\,\mathrm{km^2}$ (~16 grid cells). MCS tracking is performed from storm genesis to decay using the algorithm presented in Stein et al. (2015) by identifying contiguous regions of cold cloud that partially overlap between hourly intervals. Tracked storms are analyzed at 1800 UTC in sections 5 and 6 as this is the time of maximum modeled precipitation (see section 4). Different times of MCS occurrence have been evaluated in section 7.

Tracking MCSs using OLR instead of precipitation allows for continuous identification of large-scale organized systems even when MCS precipitation may be spatially or temporarily intermittent (Klein et al. 2018, their Fig. 4a). We have analyzed precipitation-tracked events, finding little difference in key results (not shown). The choice of a fixed temporal analysis window means that MCSs may be analyzed at times when they are not at their maximum intensity; however, we believe that this decision is fair given the availability of data as well as the complementary analysis in sections 4 and 7.

In this paper, we set two further restrictions on MCSs identification with the following rationales:

- All MCSs have an extreme rain rate at 1800 UTC greater than $10\,\mathrm{mm\,h^{-1}}$. This restriction excludes nonprecipitating cold cloud structures. The threshold of $10\,\mathrm{mm\,h^{-1}}$ is arbitrary. Different thresholds (between 5 and $30\,\mathrm{mm\,h^{-1}}$) were analyzed, with little difference in results.
- All MCSs must have mean ambient (1200–1600 UTC) precipitation rate below $1\,\mathrm{mm\,h^{-1}}$ across the region where each MCS is located at 1800 UTC. This restriction removes MCSs where the midday atmosphere is perturbed by precipitation. Use of this restriction reduces the number of MCSs analyzed (only 26% of current climate storms and 27% of future climate storms pass this criterion). Evaluation of the vertical profile of horizontal winds, and CAPE, in the environment preceding the arrival of an MCS requires an atmosphere not disturbed by the potential effects of prior storms. Complementary analysis for all MCSs regardless of this restriction shows similar findings to those given here (not shown).

There are 1020 current climate MCSs and 553 future climate MCSs that meet both criteria. The fact that CP4-A projects fewer Sahelian MCSs in the future climate fits with prior analysis (cf. Riede et al. 2016). Berthou et al. (2019a) and Kendon et al. (2019) additionally show that CP4-A simulates fewer Sahelian rain events in the future regardless of storm size.

All metrics listed in Table 1 are calculated over the location where each MCS is present at 1800 UTC. ''Ambient'' conditions (e.g., MU-CAPE) are evaluated at 1200 UTC consistent with Taylor et al. (2017), while ''internal'' storm characteristics (such as minimum omega), are evaluated at 1800 UTC. Our choice of evaluation times allow us to examine the influence of prestorm environment and the internal storm dynamics in controlling MCS extreme precipitation rates within CP4-A. We highlight that our measure of ambient wind shear does not use fixed pressure levels to evaluate the low-level southwesterly and midlevel easterly ambient wind circulations. Rather, our shear measure captures the maximum difference between these two circulations across the lower to midtroposphere. We consider this modification of importance given that changes in surface pressure and the potential vertical displacement of the AEJ are not variables

TABLE 1. Metrics used within this study, their calculation methods, and model output availability. Metrics have been ordered based on model variable assessed. All metrics are evaluated across the region where MCSs are simulated at 1800 UTC. Where implicit in metrics name (e.g., mean precipitation rate), methodology is not described further for brevity.

Metric (units)	Time (s) assessed	Pressure level	Output availability	Method
Extreme precipitation rate ($mm\,h^{-1}$)	1800 UTC	N/A	Hourly mean	Extreme precipitation rate—99th percentile of precipitation
Mean precipitation rate ($mm\,h^{-1}$)				Precipitation volume—mean precipitation rate multiplied by MCS area
Precipitation volume (kg)				
Mean OLR ($W\,m^{-2}$)	1800 UTC	N/A	Hourly mean	
Wind shear ($m\,s^{-1}$)	1200 UTC	Lower level (ll): 925–800 hPa,	3-hourly instantaneous	Wind shear—the maximum value of $[(u_{ll} - u_{ml})^2 + (v_{ll} - v_{ml})^2]^{0.5}$ for all ll and ml. Zonal wind shear—As above using only u winds
Zonal wind shear ($m\,s^{-1}$)		midlevel (ml): 700–500 hPa		
Mean TCW ($kg\,m^{-2}$)	1200 UTC, 1800 UTC	N/A	Hourly instantaneous	Variable includes water vapor, cloud water, ice and precipitation.
Minimum omega ($Pa\,s^{-1}$)	1200 UTC, 1800 UTC	600–200 hPa	3-hourly instantaneous	
Maximum buoyancy (K)	1800 UTC	600–200 hPa	3-hourly instantaneous	Temperature at the location of minimum omega minus the mean temperature at the same pressure level.
Cold pool marker (K)	1800 UTC	1.5 m	Hourly instantaneous	1st percentile 1.5-m temperature at 1800 UTC minus mean temperature at 1200 UTC.
Most unstable parcel CAPE/CIN (J) [MU-CAPE/MU-CIN]	1200 UTC	All levels	3-hourly instantaneous	Calculated using Python package *SkewT* (https://pypi.org/project/SkewT/) using the "most unstable air parcel" method, which calculates CAPE for all pressure levels, and determines the equivalent surface parcel by adiabatic descent. Calculations of the level of free convection in Table 2 are done using the *moist_ascent()* method in *SkewT*.

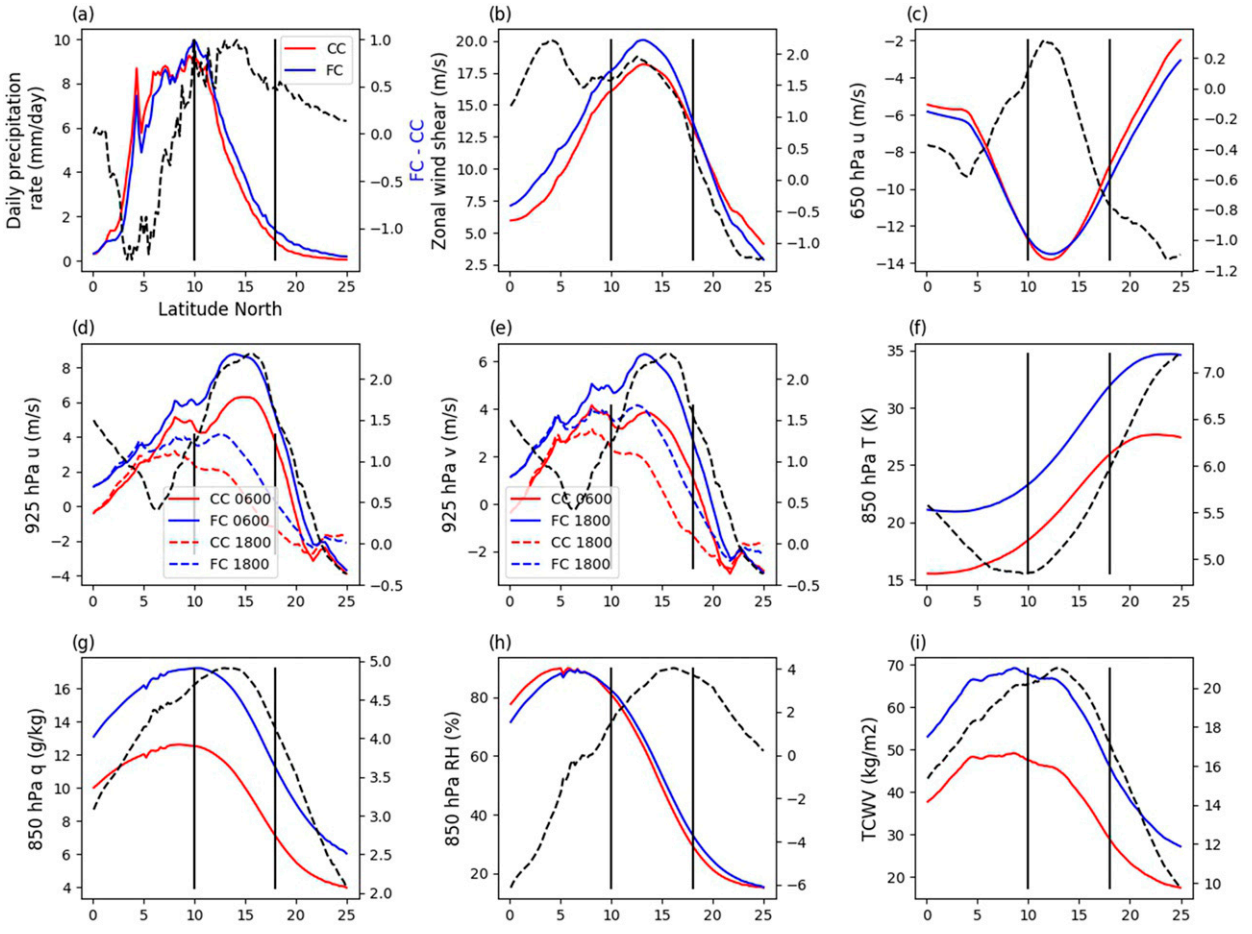

FIG. 1. Climatological change in the West African monsoon in the two CP4 climate runs. Variables plotted for July–September average across the current climate (red lines), the future climate (blue lines), as well as the difference between the two climates (black dashed lines). West African monsoon features are: (a) daily precipitation rate, (b) zonal wind shear as defined in Table 1, (c) 650 hPa zonal winds, (d) 925 hPa zonal winds, (e) 925 hPa meridional winds, (f) 850 hPa temperature, (g) 850 hPa specific humidity, (h) 850 hPa relative humidity, and (i) total column water. For all plots except (d) and (e), metrics are taken as daily averages. All metrics are zonally averaged across the region 15°W–15°E. Black vertical lines denote the latitudes of our study region (10°–18°N).

we wish to explicitly consider as potential drivers of storm intensification changes.

In our analysis, we considered both zonal wind shear (i.e., maximum low-level westerlies minus maximum midlevel easterlies) and wind shear magnitude (using both the zonal and meridional horizontal winds) (Table 1). We found little difference in the influence of either metric on extreme precipitation rates. As such, we do not show results for both metrics. Finally, due to an irreparable issue with CP4-A, 600 hPa model output is not available for the current climate storms in 1998 and some storms in 1999.

4. Climatological differences in monsoon features over the Sahel

For our analysis, a fixed geographical region has been selected for analysis across climates. However, changes in extremes may arise from shifts of the summer rain belt or other monsoon features. In this section, we consider whether the latitudes 10°–18°N offer a fair comparison of the West African monsoon across climates.

Figure 1 displays the zonally averaged (across 15°W–15°E) latitudinal change in measures of the monsoon state across climates. Mean daily precipitation (indicative of the location of the monsoon rain belt) shows similar rainfall patterns across climates with the maximum change in daily precipitation rate of $1\,\mathrm{mm\,day^{-1}}$ (Fig. 1a). There is also evidence of a northward shift of the northernmost extent of monsoon rains. Proportionally, precipitation increases are greater farther north (~40%–50% near 18°N). The ~1° northward shift of monsoon rainfall limit across climates, as well as the higher future precipitation rates over the Sahel, and a projected reduction of precipitation rates

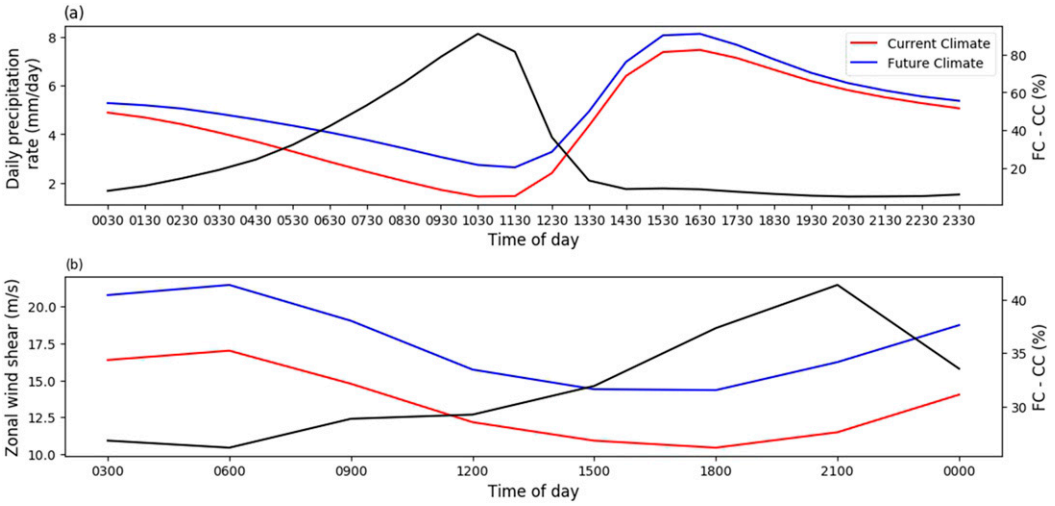

FIG. 2. Diurnal cycle of precipitation and zonal wind shear for both climates. For the region 15°W–15°E, 10°–18°N, hourly precipitation rates and 3-hourly instantaneous zonal wind shear values are averaged for the period July–September for the current climate (red line) and future climate (blue line). The difference between future climate and current climate values at each time step is represented by the black line in each panel.

near the Guinea Coast (5°–7°N) is consistent with previous studies (e.g., Vizy et al. 2013; Cook and Vizy 2015; Vizy and Cook 2017).

Mean midday zonal wind shear (Fig. 1b) increases predominantly due to stronger low-level southwesterly flow across all latitudes of around 1–2 m s^{-1} or up to 40% (Figs. 1d,e) and a relatively smaller intensification of AEJ-level easterlies across the northern Sahel of no more than 0.5 m s^{-1} (<5% across climates Fig. 1c). There is a projected latitudinal broadening of the AEJ in the future, most pronounced north of 13°N (Fig. 1c). However, the latitudinal position of peak zonal wind shear and 650 hPa winds is the same in the current and future climate simulations. Enhanced low level westerlies, indicative of the West African westerly jet diurnal peaks (WAWJ; Pu and Cook 2010, 2012), and southerlies imply an enhanced horizontal transport of moisture over the Sahel in the future.

Mean 850 hPa temperature (Fig. 1f) indicate a future increase in the meridional temperature gradient across West Africa, with temperatures increasing over the Sahara (6–7 K) more than over the Guinea Coast (5–6 K). This increased meridional temperature gradient is consistent with the enhanced zonal wind shear across the Sahel via their codependence due to the thermal wind balance (Fig. 1b; Cook 1999; Parker et al. 2005; Cook and Vizy 2015). Specific humidity (Fig. 1g) is much greater across the entire West African region in the future climate, with the difference between the two climates maximized at ~12°N. We see little (<3%) change in lower-tropospheric relative humidity between climates across the Sahel (Fig. 1h). Increased low-level southerly winds across the Guinea Coast, coupled with higher specific humidity is associated with an increase in TCW over the Sahel (Fig. 1i). The location of maximum TCW does not change across climates (9°–10°N), but the greatest absolute increase occurs within the Sahel (~12°–13°N).

The latitudinal pattern of each variable considered in Fig. 1 is consistent across climates. We conclude that the region 10°–18°N is a fair region over which to consider MCSs in both climates.

Figure 2 shows the diurnal cycle of CP4-A precipitation (Fig. 2a) and lower- to midtropospheric wind shear magnitude (Fig. 2b), averaged over our analysis region. In both climates, the maximum precipitation rate occurs during the late afternoon and is minimized around 1100 UTC. Precipitation increases at all times of day with climate change, but percentage wise, the greatest increases occur prior to 1200 UTC. CP4-A has a bias toward too much midday precipitation across the Sahel; however, the model is improved over parameterized counterpart models (Berthou et al. 2019b). Hourly rainfall rates increase by less than 20% in the future climate for all times after 1400 UTC. Kendon et al. (2019) show fewer short-lived evening storms in the future climate within CP4-A, potentially explaining the relatively small absolute/percentage increase in precipitation across the afternoon and evening period.

Observed wind shear in the lower to midtroposphere is maximized overnight, since this is the time of strongest southwesterly monsoon flow (Parker et al. 2005). The diurnal cycle of zonal wind shear is consistent across climates within our observation region (Fig. 2b). We see

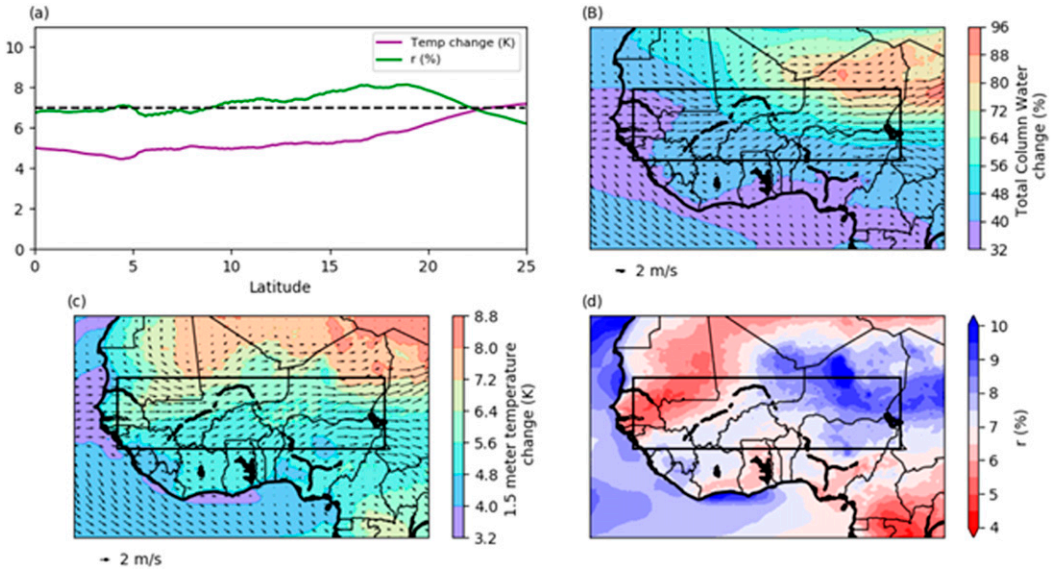

FIG. 3. Climatological changes in surface temperature, total column water, and low level horizontal winds across climates. (a) Zonally averaged climatological change in 1.5 m temperature (purple line) between the future climate and current climate scenarios. Green line displays the differential rate of change in TCW per kelvin, r, expressed as a percentage [defined in Eq. (1) and text], with the black dashed line denoting the Clausius–Clapeyron rate of 7% TCW increase per kelvin. (b) Proportional change across climates in climatological, coarse grained, TCW with absolute changes in 925 hPa horizontal winds. (c) Climatological change in coarse grained 1.5 m temperatures and 925 hPa horizontal winds. (d) Coarse grained (to 25 km horizontal resolution) map of r, expressed as a percentage change. White regions in (d) highlight areas where the increase in TCW per kelvin increase in temperature matches that predicted from the Clausius–Clapeyron equation (7% K^{-1}). For all plots, the period July–September is used to compute data shown. Black boxes in (b)–(d) denote the Sahel (10°–18°N, 15°W–15°E) as defined for our analysis.

an increase throughout the day in the percentage change of zonal wind shear across climates with a peak increase occurring at 2100 UTC (~40%). The larger percentage increase at 1500–2100 UTC is due in part to these times corresponding to the diurnal minimum in shear values. Absolute increases in zonal wind shear range between about 3.5 m s^{-1} (at 1500 UTC) and 4.8 m s^{-1} (at 2100 UTC) (Fig. S2). Spatial changes in zonal wind shear calculated between set levels (925 and 600 hPa) are provided in Fig. S3 and highlight that zonal wind shear increases more, in absolute terms, within the eastern Sahel.

We decide that using 1800 UTC as our storm reference time is fair as 1800 UTC is shortly after the time of maximum area-averaged precipitation in both climates and aligns with available instantaneous data for wind speed and temperature. However, there exist regions where overnight rainfall provides the majority of local precipitation over the Sahel (Mathon et al. 2002; Vizy and Cook 2018). Drivers of MCS extreme precipitation rates at 0000 and 0600 UTC storms are discussed in section 7.

We next consider changes in TCW and their relationship to near-surface temperature changes across climates and compared them to the expected rate of change in TCW per unit warming from the Clausius–Clapeyron relationship (i.e., 7% K^{-1} warming). We use the differential rate of TCW change per kelvin, r, expressed as a percentage change, from O'Gorman and Muller [2010, their Eq. (2)] (Fig. 3a):

$$r = 100 \times \frac{\log(1 + r_{\Delta})}{\Delta T}, \tag{1}$$

where ΔT is the mean 1.5 m temperature difference across climates, and r_{Δ} is the fractional rate of TCW change per kelvin, calculated as

$$r_{\Delta} = \frac{\mathrm{TCW}_{\mathrm{future}} - \mathrm{TCW}_{\mathrm{current}}}{\mathrm{TCW}_{\mathrm{current}}}. \tag{2}$$

Figure 3 also displays spatial maps of projected TCW, 1.5-m temperature, and near surface circulation changes across climates (Figs. 3b,c) and r as defined in Eq. (1) (Fig. 3d).

Figure 3a shows that climatological 1.5 m temperatures increase by 4–5 K near the Guinea Coast (0°–5°N), and by over 6 K across the Sahara (north of 20°N). CP4-A simulates zonally averaged $r > 7\%\ K^{-1}$ from 10° to 20°N, implying super–Clausius–Clapeyron scaling of TCW occurs across our analysis region (although the scaling is zonally heterogeneous as seen in Fig. 3d).

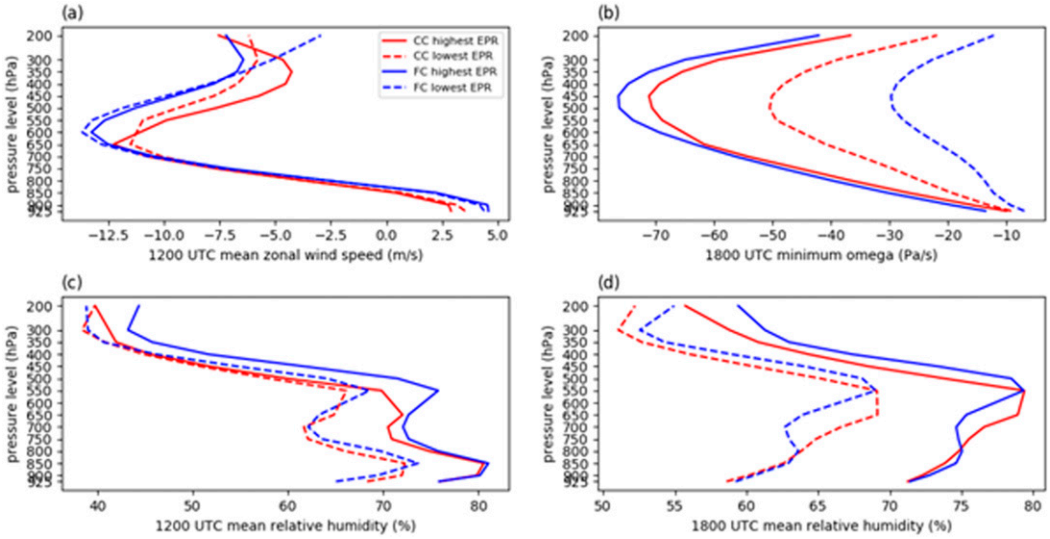

FIG. 4. Composite vertical profile of selected potential storm intensity metrics for MCSs with the highest and lowest extreme precipitation rates (EPRs). Variables displayed are (a) 1200 UTC zonal wind speed, (b) 1800 UTC minimum omega, (c) 1200 UTC mean relative humidity, and (d) 1800 UTC mean relative humidity. Composites are made for MCSs with the highest 10% of EPRs (solid lines) and lowest 25% of EPRs (dashed lines) in each climate. Red lines present results for the current climate, with future climate findings given in blue.

Consistent with Vizy et al. (2013), we see projected enhancement of the WAWJ across Senegal and southern Mali, and increased southwesterly monsoon flow across Benin, Burkina Faso, and Nigeria. Both these circulation changes would be expected to increase low-level moisture across the eastern Sahel. Accordingly, there is an apparent southwesterly gradient in the percentage TCW increase between the current and future climate (Fig. 3b). Across much of the eastern Sahel, there is >50% more moisture in the future climate. Toward Senegal, the increase is 30%–40%. Changes in surface temperature across climates appear relatively more zonally homogeneous across West Africa (Fig. 3c).

CP4-A projects super–Clausius–Clapeyron increases in r projected across the eastern Sahel, as well as Guinea, Liberia, and Sierra Leone (Fig. 3d). This high increase in TCW per K warming is of particular interest over the Niger–Nigeria border, as this is a location where many observed MCSs originate during the boreal summer (Vizy and Cook 2018, 2019) and occur in the current climate CP4-A simulation. Sub–Clausius–Clapeyron r values over Senegal and Mauritania are due to strengthened northerlies from the increased low-level cyclonic circulation about the deepened trough providing warming and drying in over this region. The zonal contrast in simulated r presented in Fig. 3d is consistent with projected CP4-A increases in extreme precipitation across the Sahel (Kendon et al. 2019), currently observed spatial heterogeneity in precipitation trends (Panthou et al. 2018), and spatial patterns of seasonal precipitation change from other future climate studies using coarser-resolution models (e.g., James et al. 2014; their Fig. 1).

In conclusion, we find an intensification of climatological precipitation across much of our study region present at all times of day. There is an increase in zonal and horizontal wind shear in the future climate, primarily associated with a strengthening of the low-level monsoon flow and the WAWJ, with a relatively smaller intensification of the AEJ apparent. Zonally averaged low-level specific humidity and TCW increase in the future. There is a spatial heterogeneity to the increase in available moisture for MCSs relative to localized heating, which is spatially consistent with prior studies highlighting zonal contrasts in current and future precipitation trends over the Sahel.

5. Changes in storm intensity and drivers within and across climates

a. Vertical profile of storm environment: Dependence on intensity and climate

We next investigate whether selection of fixed pressure levels for comparison of storm drivers across climates is valid, or whether considerations for vertical displacement of storm intensity drivers must be taken into account. Figure 4 displays the vertical profile of mean midday zonal wind speed (Fig. 4a), 1800 UTC minimum omega (Fig. 4b), and relative humidity at 1200 UTC (Fig. 4c) and 1800 UTC (Fig. 4d) for storms

with the highest and lowest extreme precipitation rates in each climate.

At 925 hPa, we see stronger composite low-level westerlies preceding storms with the lowest 25% of extreme precipitation rates in the current climate simulations (Fig. 4a, ~1 m s^{-1} difference). Stronger composite ambient westerly winds are simulated at this level in the future climate compared to the current climate, but we do not see a difference between ambient westerlies preceding MCSs with the highest and lowest extreme precipitation rates.

More intense easterlies at 650 hPa precede MCSs with higher extreme precipitation rates in the current climate with easterlies approximately 1 m s^{-1} more intense. At higher levels, current climate ambient easterlies are weaker preceding MCSs with the highest extreme precipitation rates. We also note that composite 650 hPa easterlies preceding both subsets of current climate MCSs are actually weaker than those preceding the all-storm composite at 650 hPa (not shown). In the future climate, we see enhanced mid and upper tropospheric easterly flow preceding both subsets of storms, with the strongest composite easterlies from 650 hPa upward simulated prior to MCSs with the lowest extreme precipitation rates. In both climates, Fig. 4a implies that enhanced ambient zonal-wind shear may not be present prior to systems with higher extreme precipitation rates. As an aside, when storm intensity is measured using mean OLR, we do see a clear pattern toward more intense midlevel easterly winds preceding colder-topped MCSs (Fig. S4a). For the remainder of our analysis, set pressure ranges across which to evaluate lower-tropospheric westerlies (925–800 hPa), and midtropospheric easterlies (700–500 hPa) for both climates are considered fair.

In both climates, MCSs with higher extreme precipitation rates have higher composite minimum omega at the time of storm throughout the mid and upper troposphere compared to those with lower extreme precipitation rates (Fig. 4b). For storms with the highest extreme precipitation rates in either climate, composite omega values are similar between climates below 600 hPa with stronger omega simulated higher than 600 hPa in the future, implying greater in-storm ascent rates. The opposite is true for events with the lowest extreme precipitation rates, as current climate storms are simulated to have more intense in-storm omega. Figure 4b implies relatively more extremes (both strong and weak) of in-storm ascent rates simulated for future climate MCSs. Through the rest of this article, we use minimum omega above 600 hPa for each MCS as the indicator of maximum speed of ascending air in MCS convective cores (while appreciating that the grid resolution of our model reduces the precision of this measurement).

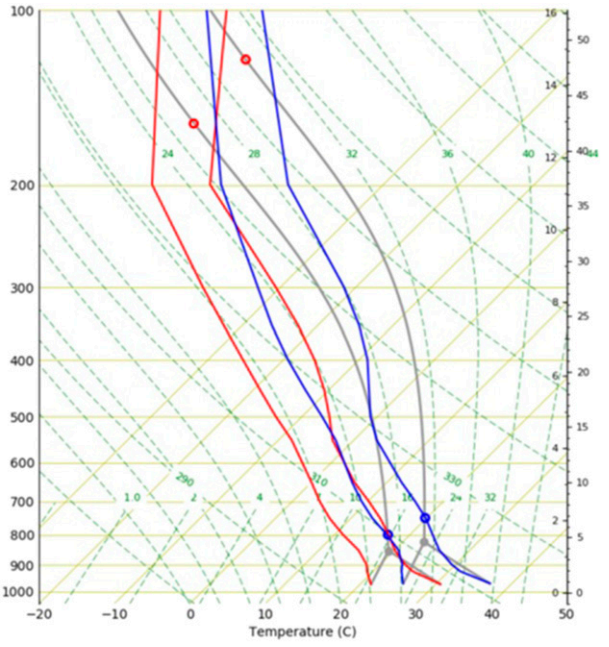

FIG. 5. Composite skew T–log$p$ diagram of ambient conditions preceding all storms found in the current climate (red lines) and the future climate (blue lines). For each profile, blue filled circle represents the level of free convection of a surface-based air parcel, while red open circle represents the pressure of the equilibrium level. For each profile, 600 hPa data have been omitted due to errors at this level for all 1998 and some 1999 storms.

We see a clear separation between composite RH profiles for MCSs with the largest extreme precipitation rates and lowest extreme precipitation rates for a given climate (Fig. 4c for 1200 UTC, Fig. 4d for 1800 UTC). In either climate, higher 1200 UTC relative humidity values are simulated below about 550 hPa preceding storms with higher extreme precipitation rates (Fig. 4c), with higher 1800 UTC RH values simulated throughout the vertical column (Fig. 4d). Across climates, we see little change in 1200 UTC composite low-level RH for either MCS subset, but greater mid to upper tropospheric humidity preceding MCSs with the highest precipitation rates in the future climate. At the time of storm, there is a consistent simulated drying of the lower- to midtroposphere simulated for future climate storms (~800–600 hPa) for both respective MCS populations. For the rest of this paper, we evaluate 1200 UTC RH in order to focus on the influence ambient conditions have on extreme precipitation rates, and select 700 hPa as a representative pressure level for analysis of midtropospheric RH.

Figure 5 shows the skew T–log$p$ plot of composite profiles preceding current climate (blue lines) and future climate (red lines) storms; Table 2

TABLE 2. Composite values related to the vertical profiles shown in Fig. 5.

Variable	Future climate composite ambient climate	Current climate composite ambient climate
Mean surface pressure (hPa)	968.5	971.3
Mean surface temperature (°C)	37.1	30.6
Mean dewpoint temperature (°C)	25.6	21.4
Pressure of lifting condensation level (hPa)	822.0	850.5
Temperature at lifting condensation level (°C)	22.9	19.3
Pressure of level of free convection (hPa)	744.9	796.3
Pressure at equilibrium level (hPa)	121.3	156.3
CAPE of most unstable parcel (J)	3378.6	2463.7
CIN of most unstable parcel (J)	−31.3	−11.4

provides relevant statistics from these soundings. Future storms are preceded by higher equilibrium and lifting condensation levels, and greater ambient bulk CAPE and bulk CIN, which are expected to favor more intense deep convection. The higher CIN environment seen in the future climate suggests that stronger triggers (such as cold pools) are required to initiate deep convection in this environment, consistent with the greater preponderance of nocturnal propagating systems, as compared with scattered evening cumulonimbus.

b. *Character of extreme storms and prestorm environment in current and future climate*

Figure 6 compares populations of current climate and future climate ambient/time-of-storm metrics. Changes between climates are statistically significant beyond the 90th–99th percentile for all metrics apart from 1800 UTC minimum omega (Fig. 6h). Figure 6a shows a 28% increase of mean extreme precipitation rates under climate change. Future climate storms are on average deeper, with higher rain rates, but have warmer cloud tops (Fig. 6g) due to a warmer troposphere (Fig. 5).

We find intensifications in mean 1200 UTC wind shear (Fig. 6b), 1800 UTC mean TCW (Fig. 6c), and ambient bulk CAPE of the most unstable air parcel (Fig. 6e) as well as drier ambient midlevel air (Fig. 6f). Relative to the large increase in mean 1800 UTC TCW across climates (41%), we see a smaller, but significant increase in the 1200–1800 UTC TCW anomaly across climates (21%, Fig. 6d). One-hour total precipitation accumulation increases in the future climate (Fig. 6j), as well as the temperature deficit of cold pool outflows (Fig. 6l). The future change in 1-h precipitation accumulation is not linked to larger storms in the future; in fact there are fewer large storms in the future climate (Fig. 6k). Figure 6 highlights a significant shift in the CP4-A future climate scenario toward conditions conducive to more intense rain events.

6. Storm-level dynamics and intensity drivers in the current and future CP4-A simulations

a. *What controls extreme precipitation rates in CP4-A?*

Figure 7 shows the relationships between different ambient and internal variables and modeled extreme precipitation rates for both climates. There is no statistically significant (at the 95% confidence interval) correlation between future climate ambient wind shear and extreme precipitation rates, with a weak yet significant negative correlation between the same metrics seen for the present climate (Fig. 7a). The relationship between the vertical profile of lower- to midtropospheric ambient winds and extreme precipitation rates is complex, with observational and modeling studies highlighting different potential relationships (cf. Takemi 2014 and Taylor et al. 2017). The correlations shown in Fig. 7a agree with prior studies performed using CRMs (e.g., Lucas et al. 2000; Takemi 2010, 2014), but disagree with Fig. S1.

Time of storm TCW and vertical velocity exhibit the strongest control on extreme precipitation in either climate (Figs. 7b and 7d respectively), with the product of these two variables, an approximation for water uplift in the most intense convective core, also significantly scaling with extreme precipitation rates (not shown). Additionally, Taylor et al. (2017) hypothesized that more intense systems supply increased moisture. Figure 7c agrees with this notion with good agreement between the correlation of extreme precipitation rate and TCW anomaly at 1800 UTC across climates. However, this model result could be coincidental, with intense storms forming in large-scale environments that generate increases of TCW between 1200 and 1800 UTC for unrelated reasons.

Colder-topped MCSs have higher extreme precipitation rates in both climates consistent with expectations (Fig. 7e). Lower MU-CAPE (Fig. 7f) and more humid

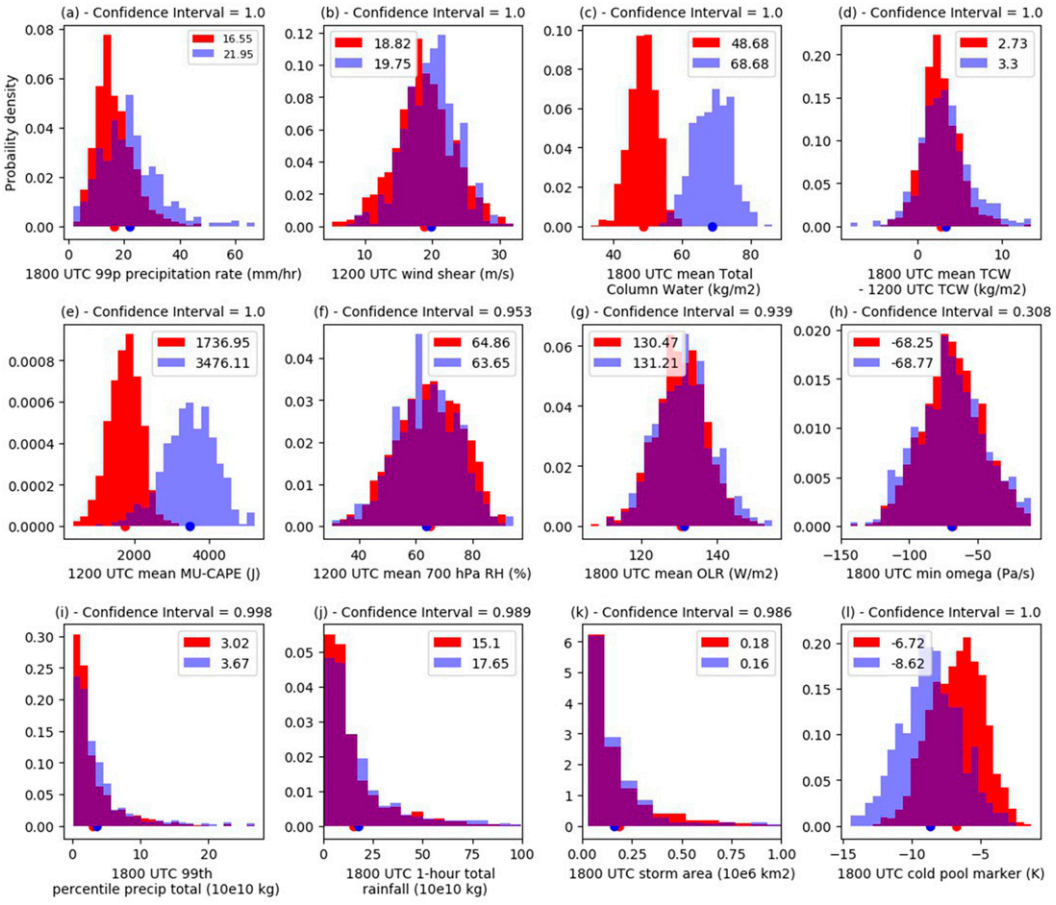

FIG. 6. Probability density functions of extreme precipitation rates during MCSs within both climates and identified atmospheric/storm variables of interest. In all plots, red bars highlight the binned probability density in the current climate, with blue bars denoting future climate values (dark blue bars exist where current and future climate values overlap). All values are taken across the identified region of each MCS at 1800 UTC as explained in section 3. In all panels, red (blue) dots below the vertical bars denote the climatological mean value of each metric for the current (future) climate which are also presented in each subplot legend. Confidence intervals are calculated from a Welch's *t* test for the two populations.

ambient midlevels (Fig. 7g) are significantly correlated with higher extreme rain rates. We stress that MU-CAPE as defined in Table 1 is not directly comparable to the depth of high CAPE air within the lower-troposphere analyzed in Takemi (2010, 2014). It is important also to note that the processes through which increased MU-CAPE can affect precipitation may be crudely modeled at 4.4 km horizontal resolution, given the potential influence of cloud-mixing and microphysical processes. Other measures of CAPE, including for surface-based parcels and the mean parcel CAPE in the lowest 100 hPa of the atmosphere, have also been evaluated, with little difference in their relationship with precipitation rates.

Storms with higher extreme precipitation rates in either climate output greater quantities of rainfall during 1 h across the entire MCS area (Fig. 7h), implying these systems potentially have broad impacts over the regions they are present. Finally, there is no significant correlation between cold pool intensity and extreme precipitation rate in either climate (Fig. 7i). Although intense storms can be associated with strong cold pools, ice hydrometeor melting, sublimation, and evaporation help generate cold pools, which can correspond to minimal precipitation at the surface.

As discussed in section 2, our two 10-yr simulations are each affected by the models own internal natural variability. We note however that the natural variability in each run is constrained by the lower and lateral boundary conditions. To quantify the potential influence of long-time scale variability on ambient TCW, we have compared the change in June–September TCW from a historical period (1950–99) to the end of the twenty-first century (2070–99) within a four-member

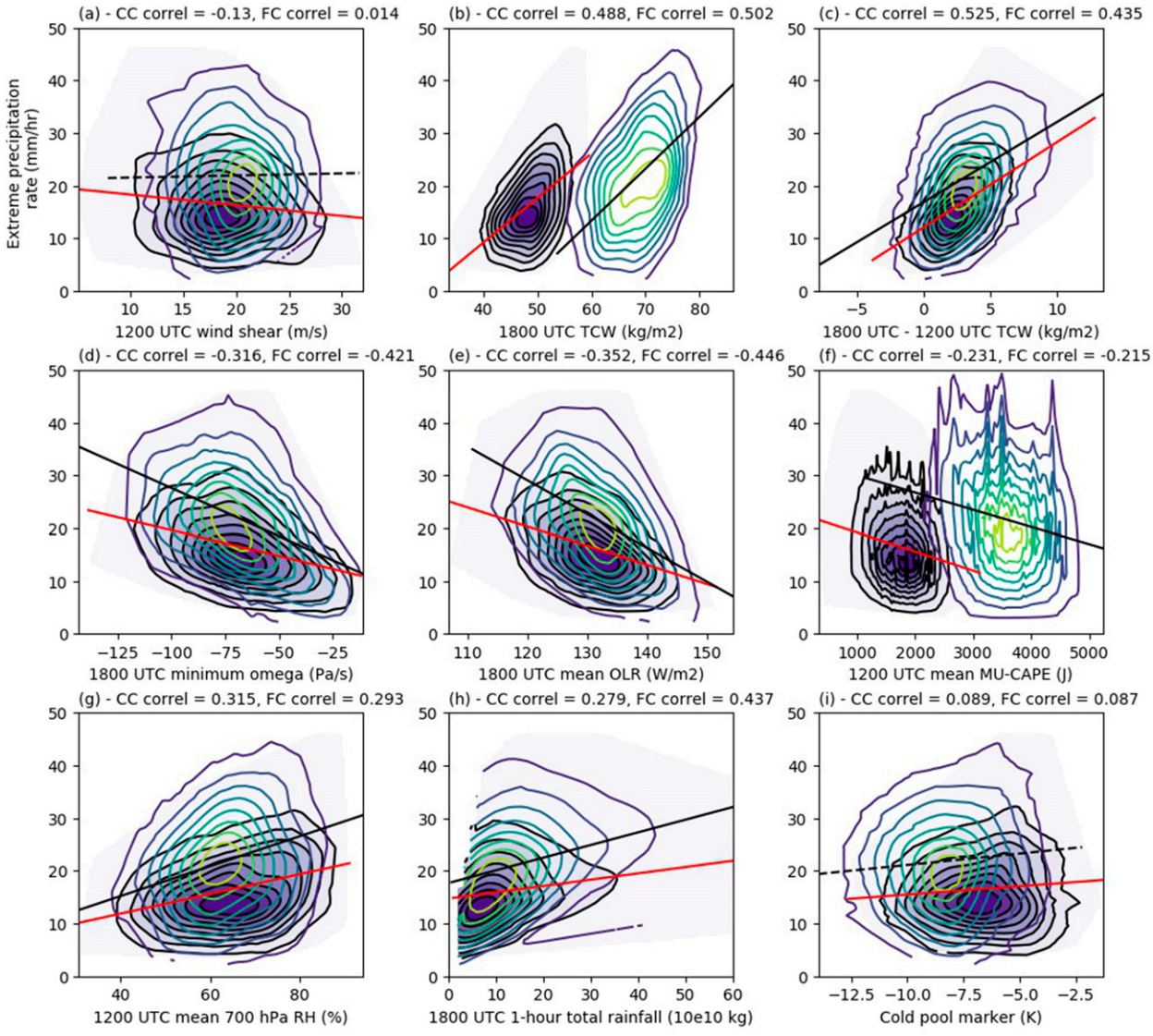

FIG. 7. Weighted density contour relationships between extreme precipitation rates and potential drivers in current and future climates. (a)–(i) The relationship for all current climate (black contours) and future climate (colored contours) MCSs. Pale gray shading denotes the total current climate range including anomalous results. For each variable linear trend lines for each climate as well as the Pearson correlation coefficient are provided (black line for future climate, red line for current climate). Solid lines of best fit denote correlations significant beyond the 95th confidence interval.

GCM ensemble using a single model (HadGEM2-ES) forced with different initial conditions following RCP8.5. HadGEM2-ES is employed as it provides the best comparison to CP4-A given similarities in model design.

Historic climatological TCW values over the Sahel range from 30.3 to 30.6 kg m^{-2} across ensemble members; future values range from 46.3 to 47.1 kg m^{-2}. The difference in TCW across climates (~16 kg m^{-2}) is comparable to the difference in TCW simulated in CP4-A (Fig. 7b). Interensemble variability in each climate is much lower than the change projected across climates, implying that the TCW differences projected in CP4-A are likely associated with climate change and not a product of random variability.

b. *Modeled interactions of storm intensity drivers in CP4-A*

Figure 8 shows the relationships between selected ambient and time of storm metrics. Figure 8a shows a significant negative correlation between midday wind shear and mean time-of-storm OLR in both climates. The correlation coefficients are of similar magnitude to that found in observations (Taylor et al. 2017; their coefficient: −0.347), suggesting that CP4-A captures the

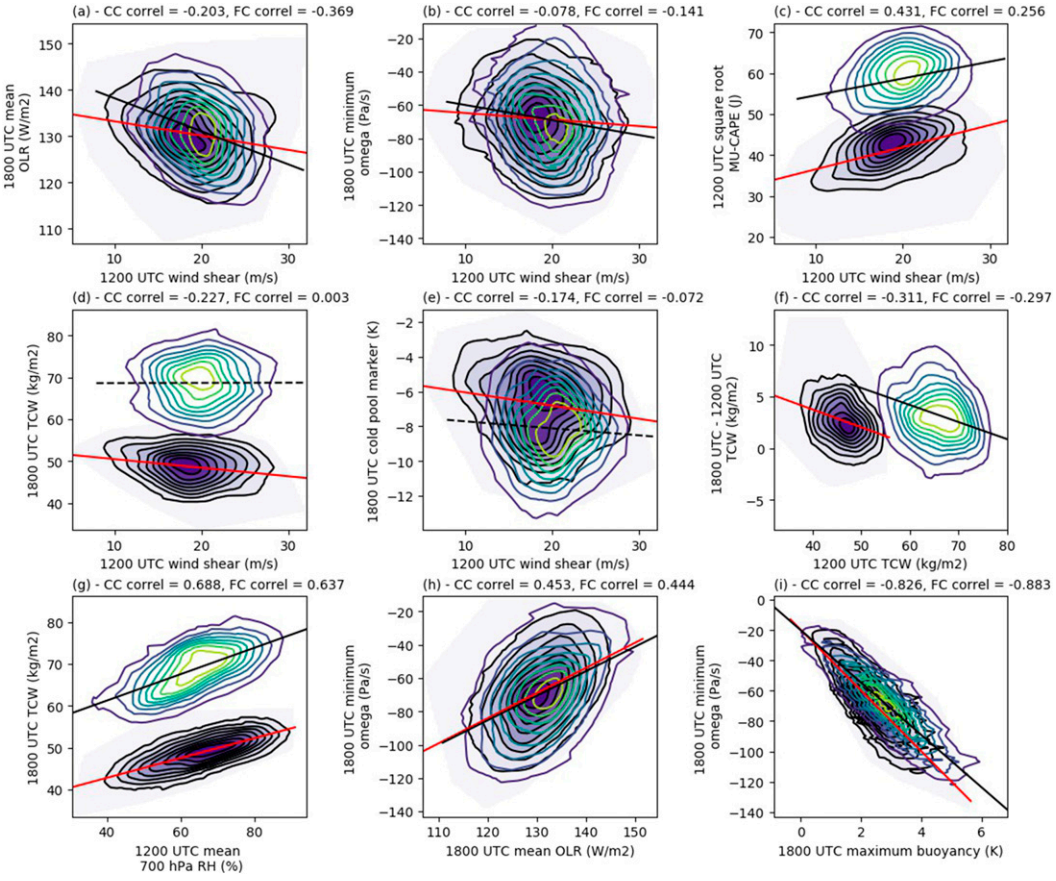

FIG. 8. Weighted density contour relationships between potential drivers of extreme precipitation in current and future climates. (a)–(i) The relationship for all current climate (black contours) and future climate (colored contours) MCSs. In each panel linear trend lines for each climate as well as the Pearson correlation coefficient are provided (black line for future climate, red line for current climate). Solid lines of best fit denote correlations significant beyond the 95th confidence interval. The variables shown are: (a) midday wind shear and time of storm OLR, (b) midday wind shear and 1800 UTC minimum omega, (c) midday wind shear and the square root of mean midday MU-CAPE, (d) midday wind shear and time of storm TCW, (e) midday wind shear and time of storm cold pool strength, (f) midday mean TCW and 1800 UTC–1200 UTC TCW anomaly, (g) midday mean 700 hPa RH and time of storm TCW, (h) time of storm mean OLR and minimum omega, and (i) time of storm maximum buoyancy and minimum omega.

observed influence of ambient wind shear on MCS organization. The role of shear in determining the structure and organization of MCSs has also been identified in observational studies and studies using CRMs (e.g., Newton 1960; Browning and Ludlam 1962; Rotunno et al. 1988; Houze 2004; Takemi 2007). We additionally note that, for a given temperature and humidity profile, there may exist a vertical wind profile which optimizes MCS organization (Takemi 2007). Across climates, the horizontal winds, humidity and temperature significantly change in CP4-A (Fig. 1) implying that the future climate ambient environment may be more conducive to MCS organization once a storm is generated.

Within the range of simulated wind shear values, we see a weak but significant correlation between ambient shear and in-storm minimum omega (Fig. 8b), which agrees with prior studies (e.g., Fovell and Ogura 1989; Lucas et al. 2000). In each climate, ambient wind shear is also correlated with 1200 UTC MU-CAPE (Fig. 8c). This link may be cofluctuation not causation, may be due to intense shear in the lower troposphere inhibiting convective initiation, or may be due to the presence of enhanced low-level convergence in high shear environments. Ambient wind shear is either significantly negatively correlated (in the current climate: −0.227 correlation coefficient), or not correlated (in the future climate: 0.003 correlation coefficient) with time-of-storm TCW (Fig. 8d).

Both climates simulate stronger wind shear preceding MCSs with more intense cold pools, however this

relationship is only statistically significant in the current climate (Fig. 8e). Past studies have highlighted the importance of wind shear in controlling cold pool strength (Thorpe et al. 1982; Rotunno et al. 1988), but this relationship is complex (Parker 1996). Prior research has also highlighted ambiguity with the role of other ambient conditions such as dry midlevels in intensifying convective cold pools (James and Markowski 2010). Detailed analysis of cold pool simulations for CP4-A storms is beyond the scope of this paper. However, our analysis implies that the factors required to sustain a strong cold pool are likely to be prohibitive to higher extreme precipitation rates in CP4-A.

Figure 8f implies that systems preceded by higher ambient TCW have statistically significant lower 1200–1800 UTC TCW increases in both climates. As in Fig. 7c, the correlation coefficient between these two variables is consistent across climates, suggesting that the fundamental behavior of MCSs with regards to available moisture does not change under global warming. In both climates we also note that higher time-of-storm TCW is significantly correlated with increased midtropospheric RH with similar correlation coefficients (~0.65) found for each climate (Fig. 8g). The maximum vertical velocity of MCSs is significantly correlated with mean OLR in both climates (Fig. 8h). Finally, the maximum buoyancy of rising air parcels simulated for each MCS is closely tied to the uplift velocity (Fig. 8i) implying a realistic relationship between buoyancy and upward motion is simulated within CP4-A.

Figures 7 and 8 suggest that current- and future-climate storms simulated within CP4-A behave similarly. Ambient wind difference exhibits control on the organization of developing systems, with higher wind difference associated with colder MCS cloud tops, potentially through the ability of lower- to midtropospheric wind shear to control the verticality of ascending air within a system and the buildup of CAPE. Higher TCW and ascent rates at the time of storm are closely associated with greater extreme precipitation rates, with the product of these two variables showing good correlation with extreme precipitation rates. Although it may be expected that time-of-storm TCW correlates with precipitation metrics (as precipitation can only fall if there is precipitable water available, and precipitation actually contributes a small fraction of the TCW), it is of interest that TCW is the strongest control of the selected potential drivers of extreme rain rates within CP4-A both in each climate, and across climates.

Stronger ambient wind shear is associated with stronger cold pools in the current climate (Fig. 8e), thus encouraging gregarious development of MCSs, and stronger ascent rates in both climates, implying faster uplift of moisture. However, wind shear is also associated with lower TCW and higher MU-CAPE, and therefore may also negatively impact extreme precipitation rate. Our results imply that there is no simplistic direct relationship between ambient wind shear and extreme precipitation rates in CP4-A for either climate.

Under global warming, the atmosphere becomes more conducive to higher extreme precipitation rates for early evening MCSs, however less favorable overall to MCS genesis (Berthou et al. 2019a). With regard to changes in extreme precipitation rates, the key climatic difference is the 41% increase in time-of-storm TCW, which is attributable to both an increase in ambient (i.e., 1200 UTC) TCW, and greater 1200–1800 UTC TCW. This increase in the afternoon increase in TCW may be generated by developing MCSs, may simply reflect the greater availability of TCW in the future climate which has a diurnal variation, or may reflect a change in that diurnal cycle (we do not investigate further here). From Fig. 3, we note that the eastern Sahel is projected to have super–Clausius–Clapeyron scaling of TCW with temperature; accordingly this region sees the largest frequency of future climate MCSs (not shown).

Figures 1 and 3 highlighted zonal and meridional heterogeneity in the projected change of several storm intensity drivers, notably TCW and CAPE. The analysis presented in Figs. 7 and 8 has been reproduced for the western Sahel (15°W–0°, Figs. S5 and S6), and the eastern Sahel (0°–15°E, Figs. S7 and S8), as well as over more constrained latitudinal bounds (11°–12°N, Figs. S9 and S10; 16°–17°N, Figs. S11 and S12). We draw similar conclusions to those presented above for MCSs within either the west or east Sahel as well as those present across 11°–12°N. For MCSs found over 16°–17°N, we find that their behavior is very similar to the all-storm analysis (cf. Fig. 8 and Fig. S12); however, ambient CAPE and midlevel RH do not appear to be significant drivers of extreme precipitation rate variance in either climate for these events (Fig. S11). Although the interaction of storm processes remains similar throughout the Sahel region studied, latitudinal variations in humidity and available energy can affect the relationship between these metrics and extreme precipitation rates.

7. Change in correlation of storm drivers for different intensity measures, and at 0000 and 0600 UTC

In section 6, we consider drivers of extreme precipitation rates of early evening MCSs across the Sahel. Here, we extend our analysis to consider drivers of

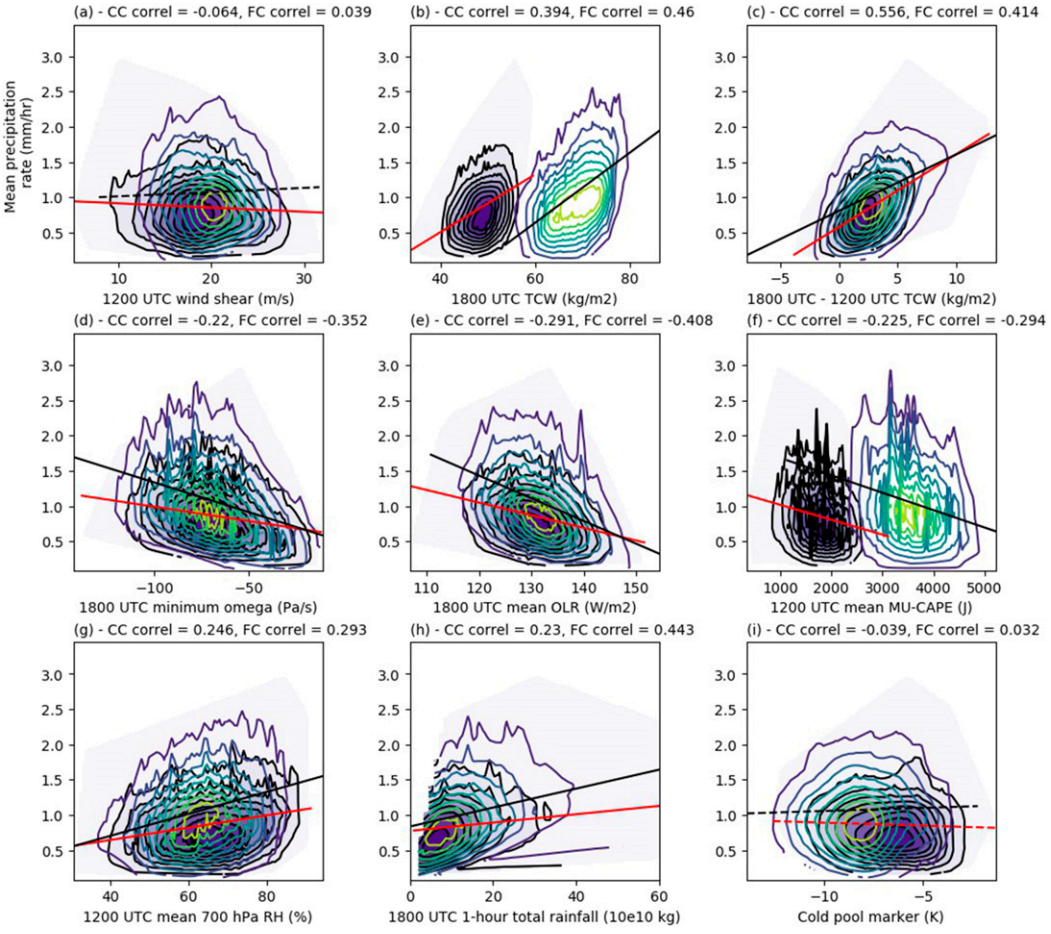

FIG. 9. As in Fig. 7, but using mean precipitation rate of 1800 UTC storms as a measure of MCS intensity.

mean precipitation rate change across climates, as well as drivers of extreme precipitation rate changes for nocturnal MCSs. This analysis is necessary, as prior work has suggested that mean MCS precipitation rates are controlled by ambient/internal drivers different from those which affect extreme precipitation rates (Takemi 2010), and different storm intensity drivers are present at different times of day (Vizy and Cook 2018).

Figure 9 displays analogous information to Fig. 7, except for mean precipitation rates. We note the caveat that Fig. 9 does not account for changes in MCS area across climates.

The drivers of extreme precipitation rate and mean precipitation rate variability within the current climate and future climate simulations are broadly similar. For both measures of early-evening precipitation, increased ambient wind shear does not have a significantly positive effect [panel (a) of both figures]. Increased time-of-storm TCW and 1200–1800 UTC TCW increases show the strongest correlation with mean precipitation rates across both the current and future climates (Figs. 9b,c). MCSs with higher mean precipitation rates have significantly stronger minimum omega (Fig. 9d) and significantly colder mean OLR (Fig. 9e), consistent with Fig. 7. Figure 9f implies that increased CAPE is significantly negatively correlated with mean precipitation rates within both climates. This result is seemingly at odds with Takemi (2014), who highlight the importance of increased depth of high CAPE in the lower troposphere. However, the effect of latitudinal variations in CAPE cannot be discounted as a cause for this difference (as seen in section 6), nor can differences in methodology for evaluating CAPE. A more thorough investigation of the spatial and vertical distribution of CAPE in the lower troposphere simulated in CP4-A prior to MCSs of different intensities is beyond the scope of this study, but will form the basis of future work.

Drivers of extreme precipitation rates of MCSs at 0000 UTC (Fig. 10) are similar to those found for 1800 UTC extreme precipitation rates. Note that for

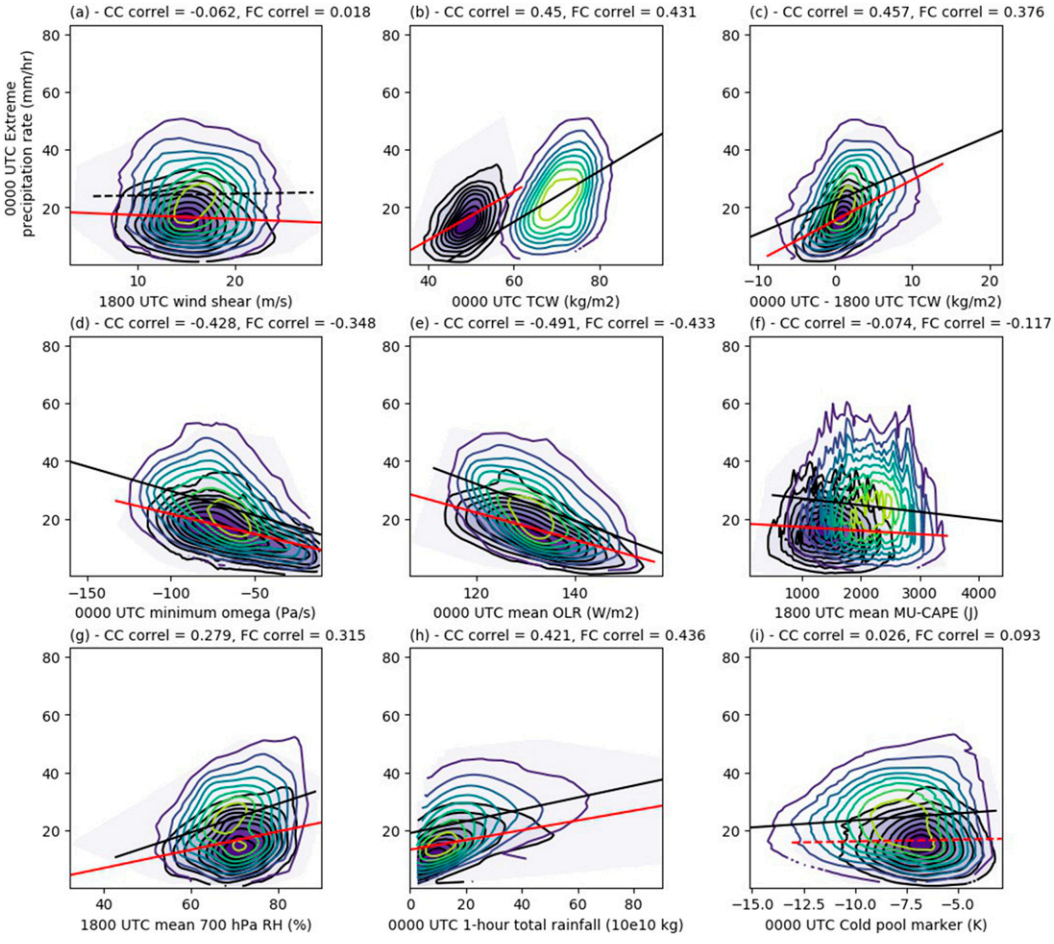

FIG. 10. As in Fig. 7, but measuring drivers of extreme precipitation rate for storms at 0000 UTC.

0000 UTC MCSs, we consider ambient conditions at 1800 UTC, and apply criteria akin to those for 1800 UTC MCSs with adjusted time windows. The quantity of ambient TCW (Fig. 10b), the 1800–0000 UTC increase in TCW (Fig. 10c), and the minimum omega within each MCS (Fig. 10d) are the predominant controls on extreme precipitation rate variability at this time.

At 0600 UTC, there is a large decline in the number of future climate MCSs simulated that meet our preset areal threshold (approximately 400 MCSs) and both our preset precipitation criteria (29 MCSs). Figure 11 therefore shows all MCSs of at least 25 000 km^2 that are preceded by ambient mean precipitation not exceeding 1 $cm\,h^{-1}$ rather than 1 $mm\,h^{-1}$. Using this relaxed restriction allows for 354 storms to be evaluated for the future climate, and 1307 to be evaluated for the current climate.

Although different MCS triggering mechanisms have been highlighted for early evening and nocturnal systems in observations (Vizy and Cook 2018), the degree to which our a priori drivers affect extreme precipitation rates are reasonably consistent between 0600 UTC (Fig. 11) and 1800 UTC (Fig. 7). The one exception to this finding is the weaker link between ambient CAPE and 0600 UTC extreme precipitation rates (Fig. 11f) compared to earlier MCS analysis times. Nevertheless, we conclude from Figs. 7, 10, and 11 that CP4-A highlights the particular importance of ambient TCW, time-of-storm omega and RH for MCS extreme precipitation rate variability across the early evening and nighttime.

8. Conclusions and discussion

Using output from the first convection-permitting model of pan-African climate changes we have evaluated the processes through which global warming within a realistic future climate scenario can impact extreme precipitation rates of Sahelian MCSs, as well as the modeled drivers of change on the storm time scale. Our work is considered a climate sensitivity experiment, and the quality of projected changes is not

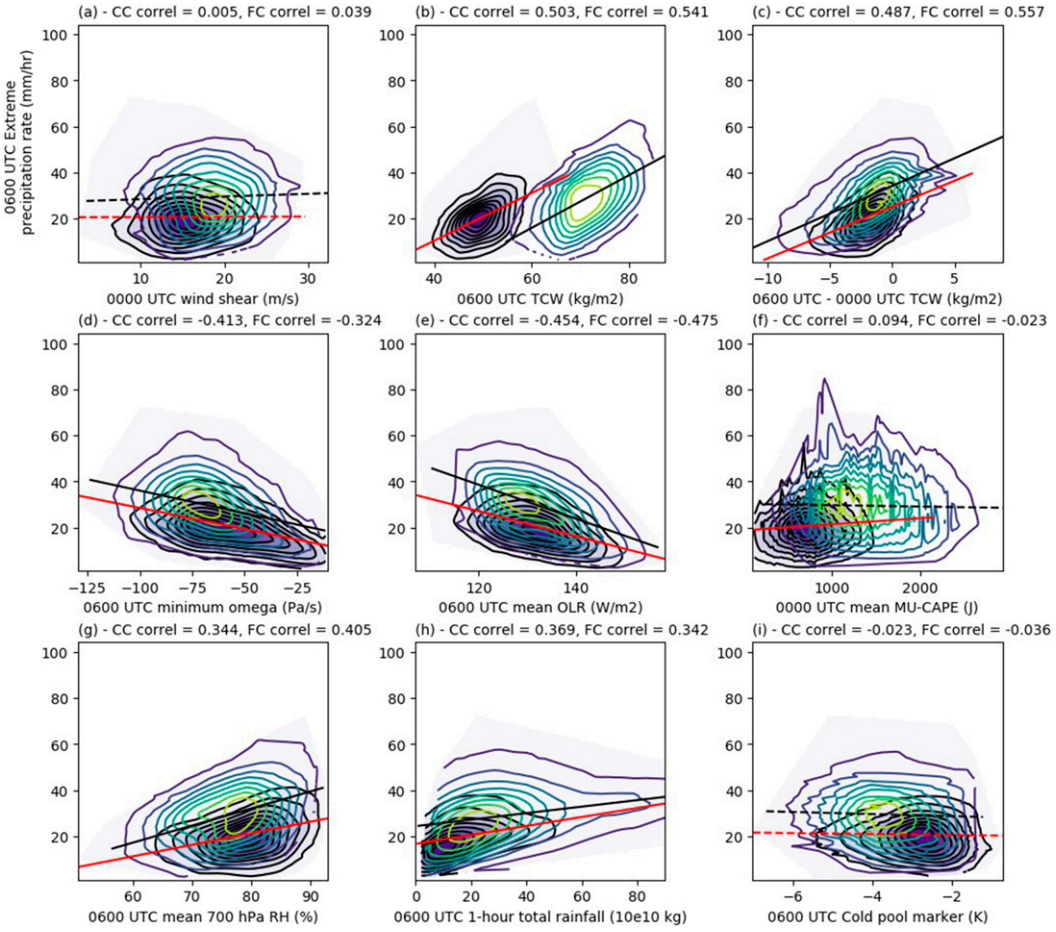

FIG. 11. As in Fig. 7, but measuring drivers of extreme precipitation rate at 0600 UTC.

assessed here. We further do not provide an evaluation of modeled precipitation against present observations as this has been assessed elsewhere (Stratton et al. 2018; Berthou et al. 2019b). Results presented primarily focus on early evening storms (1800 UTC) across the whole Sahel (10°–18°N, 15°W–15°E). Overnight precipitation systems as well as potential longitudinal and latitudinal variation in findings have been presented, with little difference in key results.

We find a 28% increase in the mean extreme precipitation rate of early evening MCSs by the end of the twenty-first century, and an increase in precipitation rates at all times of day despite fewer MCSs in the future climate. We primarily link this increase in extreme precipitation rate to increases in TCW, which scales at close to Clausius–Clapeyron scaling (although the increases have zonal heterogeneity). The greatest TCW increases are simulated across Nigeria, Niger, and Lake Chad, which corresponds to the location of most early-evening storms with particularly high extreme rain rates in the future climate. We also note that there are fewer MCSs simulated in the future climate during the early evening and overnight based on our areal threshold. Prior analysis of CP4-A output has also shown that, despite a projected increase in precipitation rates at all times of day, future rainfall over the Sahel is provided by fewer, and on average smaller systems compared to current climate precipitation (Kendon et al. 2019; Berthou et al. 2019a).

Figure 12 provides a more complete overview of modeled processes by which global warming affect user-relevant storm metrics across the Sahel within CP4-A. Figure 12 does not consider potential climate change effects due to changes in aerosols or microphysics, and as our focus is uniquely on how global and regional climate change affects rainfall, we also do not consider feedbacks of more intense MCSs on the West African climate. Figure 12 shows the following:

- Global warming increases mean temperatures across Africa as well as the temperature gradient between the Guinea Coast and the Sahara. The increased

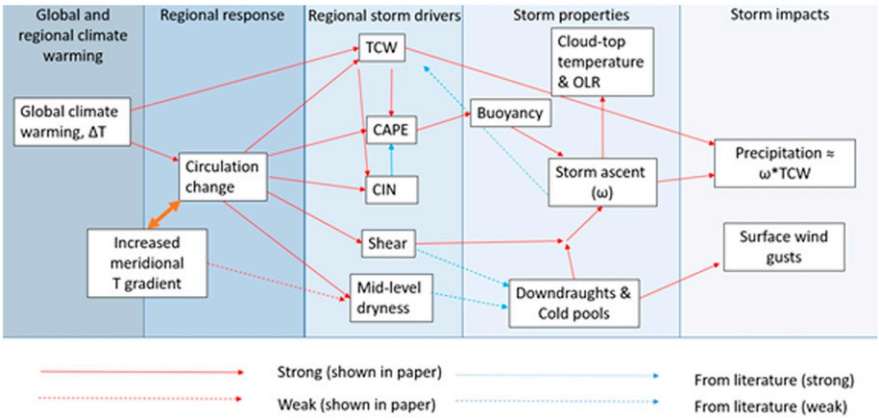

FIG. 12. Schematic diagram explaining the processes through which increases in global temperature and meridional temperature gradients across West Africa affect user-relevant storm metrics. Atmospheric drivers are separated by the scale on which they act (from global to storm-scale properties). Red lines denote correlations shown in this paper for CP4-A.

temperature gradient changes the circulation across continental West Africa, through strengthening of the southwesterly monsoon flow and an intensification of the African easterly jet and West African westerly jet (Figs. 1 and 3). The circulation change increases wind shear within the lower and midtroposphere across the region, and enhances low-level moisture flow into the Sahel.

- Water vapor mixing ratios increase approximately in line with the local temperature change to maintain constant RH at low levels (Clausius–Clapeyron scaling), but with regionally super or sub–Clausius–Clapeyron scaling as the monsoon shifts and monsoon circulation increases (Fig. 3). Across climates, the associated increases in ambient and storm-driven TCW are directly linked to enhanced extreme rain rates.
- Within each climate, increased wind shear, cold-pool strength, and in-storm buoyancy lead to an increase in updraft speeds within the storm. Moister midlevels correlate with precipitation at the surface, presumably due to increased water availability for rain formation and decreased evaporation of hydrometeors. Stronger MCS updrafts give colder cloud-top temperatures as expected, which explains the link between ambient wind shear and cloud-top temperature found in Taylor et al. (2017) and in our analysis (Fig. 8a). MCS extreme precipitation rates scale with the product of time-of-storm TCW and in-storm vertical velocity with deeper storms which bear more precipitation modeled in the future. Note that while there is no significant change in vertical velocity across climates, the distribution of vertical velocities is skewed with a longer tail of strong updrafts in the future climate simulation (Fig. 6).
- Finally, colder cold pools are simulated in the future climate. In each climate, the strength of the cold pool is significantly correlated with both near surface wind speed and wind speed cubed (a proxy for dust uplift potential; Fig. S13). However, we do not see a significant change in near surface wind speeds across climates (Fig. S14), and also note that the link between cold pool strength and wind speed weakens in the future. It is unclear why these results occur, and this subject requires future investigation.

Within CP4-A, there is no direct significant link between zonal wind shear and extreme precipitation rates, despite observational evidence suggesting such a link may exist (presented in Fig. S1). The role of zonal winds in organizing systems within the tropics is complex, and with a singular model simulation, it is not possible to ascertain the cause for this discrepancy between model and observations. Future work will explore in more detail how Sahelian MCSs develop within high and low shear environments.

The findings of this paper are both aided and limited by the novel climate model employed and some caveats to our findings are required. While the CP4-A dataset allows for interrogation of storm dynamic changes due to climate change that was not previously possible, only one future climate realization exists, and any model biases associated cannot be assessed fairly using multimodel ensembles. In particular, there is no current way to assess the impact that different future sea surface temperature anomalies would affect our findings. We hypothesize from Fig. 12 that any increase in land/ocean temperatures in the future could lead to increased extreme precipitation rates following the

processes we discuss. However, investment into more widely available and varying future climate scenarios at convection-permitting spatial resolution for West Africa would greatly help improve understanding of projected precipitation changes.

We further note that the horizontal resolution of our employed model is potentially too coarse also for conclusive insight into the role of subcloud processes (such as speed of convective updrafts) to be interpreted from our results, however do note the agreement between our findings and past observational and higher resolution modeling studies. Finally, we cannot state whether the increase in extreme precipitation rates scales linearly with increases in TCW, thus do not extrapolate our findings here to other warming scenarios or future time periods.

It is important that similar assessments to those presented here are completed for other high resolution future climate scenarios in order to more rigorously determine the balance of processes controlling enhanced precipitation rates in the future climate. From a stakeholder perspective, it is also of importance to see what changes in extreme precipitation rate could be expected for different warming scenarios in order to better advise mitigation strategies.

Data availability statement. Analysis presented within this article has been performed using Python scripts available at https://zenodo.org/record/2560410.

Acknowledgments. Fitzpatrick, Parker, Marsham, Guichard, Taylor, Crook and Rowell were supported by the Natural Environment Research Council/Department for International Development (NERC/DFID) program AMMA-2050: African Monsoon Multidisciplinary Analysis for 2050 project Grants NE/M017176/1, NE/M20126/1, and NE/M020428/1. Finney, Marsham, and Rowell were funded by the NERC/DFID funded Integrating Hydro-Climate Science into Policy Decisions for Climate-Resilient Infrastructure and Livelihoods in East Africa (HyCRISTAL). Crook was also supported by the NERC program VERA: Vegetation Effects on Rainfall in West Africa Grant NE/M003574/1. Jackson, Tucker and Stratton were supported by NERC/DFID via the FCFA funded project, Improving Model Processes for African Climate (IMPALA, NE/MO17176/1, and NE/M017214/1). Parker was also supported by a Royal Society Wolfson Research Merit Award (2014–18). Marsham was also supported by the National Centre for Atmospheric Science via the NERC/GCRF program ACREW: Atmospheric hazard in developing Countries: Risk assessment and Early Warning. Vizy, Cook, and Fitzpatrick's contributions towards this study was also funded by the National Science Foundation Award 1444505. The authors wish to extend their deepest gratitude to Margaret LeMone, the journal editor, and two anonymous reviewers for their comments, which contributed greatly to the results presented.

REFERENCES

Abel, S. J., and Coauthors, 2017: The role of precipitation in controlling the transition from stratocumulus to cumulus cloud in a Northern Hemisphere cold-air outbreak. *J. Atmos. Sci.*, **74**, 2293–2314, https://doi.org/10.1175/JAS-D-16-0362.1.

Alfaro, D. A., 2017: Low-tropospheric shear in the structure of squall lines: Impacts on latent heating under layer-lifting ascent. *J. Atmos. Sci.*, **74**, 229–248, https://doi.org/10.1175/JAS-D-16-0168.1.

Aranami, K., T. Davies, and N. Wood, 2015: A mass restoration scheme for limited-area models with semi-Lagrangian advection. *Quart. J. Roy. Meteor. Soc.*, **141**, 1795–1803, https://doi.org/10.1002/qj.2482.

Berthou, S., E. Kendon, M. J. Roberts, D. P. Rowell, S. Tucker, and R. A. Stratton, 2019a: Larger future intensification of rainfall in the West African Sahel in a convection-permitting model. *Geophys. Res. Lett.*, **46**, 13 299–13 307, https://doi.org/10.1029/2019GL083544.

——, D. P. Rowell, E. Kendon, R. A. Stratton, J. Crook, and C. Wilcox, 2019b: Improved climatological precipitation characteristics over West Africa at convection-permitting scale. *Climate Dyn.*, **53**, 1991–2011, https://doi.org/10.1007/s00382-019-04759-4.

Birch, C. E., J. H. Marsham, D. J. Parker, and C. M. Taylor, 2014a: The scale dependence and structure of convergence fields preceding the initiation of deep convection. *Geophys. Res. Lett.*, **41**, 4769–4776, https://doi.org/10.1002/2014GL060493.

——, D. J. Parker, J. H. Marsham, L. Garcia-Carreras, and D. Copsey, 2014b: A seamless assessment of the role of convection in the water cycle of the West African monsoon. *J. Geophys. Res. Atmos.*, **119**, 2890–2912, https://doi.org/10.1002/2013JD020887.

Boutle, I. A., J. E. J. Eyre, and A. P. Lock, 2014: Seamless stratocumulus simulation across the turbulent gray zone. *Mon. Wea. Rev.*, **142**, 1655–1668, https://doi.org/10.1175/MWR-D-13-00229.1.

Browning, A. J., and F. H. Ludlam, 1962: Airflow in convective storms. *Quart. J. Roy. Meteor. Soc.*, **88**, 117–135, https://doi.org/10.1002/qj.49708837602.

Cook, K. H., 1999: Generation of the African easterly jet and its role in determining West African precipitation. *J. Climate*, **12**, 1165–1184, https://doi.org/10.1175/1520-0442(1999)012<1165:GOTAEJ>2.0.CO;2.

——, and E. K. Vizy, 2015: Detection and analysis of an amplified warming of the Sahara Desert. *J. Climate*, **28**, 6560–6580, https://doi.org/10.1175/JCLI-D-14-00230.1.

Crook, J., C. Klein, S. S. Folwell, C. M. Taylor, D. J. Parker, R. A. Stratton, and T. H. M. Stein, 2019: Assessment of the representation of West African storm lifecycles in convection-permitting simulations. *Earth Space Sci.*, **6**, 818–835, https://doi.org/10.1029/2018EA000491.

Dong, B., and R. Sutton, 2015: Dominant role of greenhouse-gas forcing in the recovery of Sahel rainfall. *Nat. Climate Change*, **5**, 757–760, https://doi.org/10.1038/nclimate2664.

Dudhia, J., M. W. Moncrieff, and D. W. K. So, 1987: The two-dimensional dynamics of West African squall lines. *Quart. J. Roy. Meteor. Soc.*, **113**, 121–146, https://doi.org/10.1002/qj.49711347508.

Evan, A. T., C. Flamant, C. Lavaysse, C. Kocha, and A. Saci, 2015: Water vapor-forced greenhouse warming over the Sahara Desert and the recent recovery from the Sahelian drought. *J. Climate*, **28**, 108–123, https://doi.org/10.1175/JCLI-D-14-00039.1.

Ferrier, B. S., J. Simpson, and W.-K. Tao, 1996: Factors responsible for precipitation efficiencies in midlatitude and tropical squall simulations. *Mon. Wea. Rev.*, **124**, 2100–2125, https://doi.org/10.1175/1520-0493(1996)124<2100:FRFPEI>2.0.CO;2.

Fink, A. H., and A. Reiner, 2003: Spatiotemporal variability of the relation between African easterly waves and West African squall lines in 1998 and 1999. *J. Geophys. Res.*, **108**, 4332, https://doi.org/10.1029/2002JD002816.

Fitzpatrick, R. G. J., 2016: Analysis and prediction of the West African monsoon onset. Ph.D. thesis, University of Leeds, 319 pp.

Fovell, R. G., and Y. Ogura, 1989: Effect of vertical wind shear on numerically simulated multicell storm structure. *J. Atmos. Sci.*, **46**, 3144–3176, https://doi.org/10.1175/1520-0469(1989)046<3144:EOVWSO>2.0.CO;2.

Garcia-Carreras, L., A. J. Challinor, B. J. Parkes, C. E. Birch, K. J. Nicklin, and D. J. Parker, 2015: The impact of parameterized convection on the simulation of crop processes. *J. Appl. Meteor. Climatol.*, **54**, 1283–1296, https://doi.org/10.1175/JAMC-D-14-0226.1.

Hagos, S. M., and K. H. Cook, 2008: Ocean warming and late-twentieth-century Sahel drought and recovery. *J. Climate*, **21**, 3797–3814, https://doi.org/10.1175/2008JCLI2055.1.

Houze, R. A., Jr., 1993: *Cloud Dynamics*. Academic Press, 573 pp.

——, 2004: Mesoscale convective systems. *Rev. Geophys.*, **42**, RG4003, https://doi.org/10.1029/2004RG000150.

James, R., R. Washington, and D. P. Rowell, 2014: African climate change uncertainty in peturbed physics ensembles: Implications of global warming to 4C and beyond. *J. Climate*, **27**, 4677–4692, https://doi.org/10.1175/JCLI-D-13-00612.1.

James, R. P., and P. M. Markowski, 2010: A numerical investigation of the effects of dry air aloft on deep convection. *Mon. Wea. Rev.*, **138**, 140–161, https://doi.org/10.1175/2009MWR3018.1.

Kendon, E. J., R. A. Stratton, S. Tucker, J. H. Marsham, S. Berthou, D. P. Rowell, and C. A. Senior, 2019: Enhanced future changes in wet and dry extremes over Africa at convection-permitting scale. *Nat. Commun.*, **10**, 1794, https://doi.org/10.1038/s41467-019-09776-9.

Klein, C., D. Belušić, and C. M. Taylor, 2018: Wavelet scale analysis of mesoscale convective systems for detecting deep convection from infrared imagery. *J. Geophys. Res. Atmos.*, **123**, 3035–3050, https://doi.org/10.1002/2017JD027432.

Laing, A. G., J. M. Fritsch, and A. J. Negri, 1999: Contribution of mesoscale convective complexes to rainfall in Sahelian Africa: Estimates from geostationary infrared and passive microwave data. *J. Appl. Meteor.*, **38**, 957–964, https://doi.org/10.1175/1520-0450(1999)038<0957:COMCCT>2.0.CO;2.

Laurent, H., N. D'Amato, and T. Lebel, 1998: How important is the contribution of the mesoscale convective complexes to the Sahelian rainfall? *Phys. Chem. Earth*, **23**, 629–633, https://doi.org/10.1016/S0079-1946(98)00099-8.

Lebel, T., and A. Ali, 2009: Recent trends in the central and western Sahel rainfall regime (1990–2007). *J. Hydrol.*, **375**, 52–64, https://doi.org/10.1016/j.jhydrol.2008.11.030.

Lélé, I. M., and P. J. Lamb, 2010: Variability of the Intertropical Front (ITF) and rainfall over the West African Sudan-Sahel zone. *J. Climate*, **23**, 3984–4004, https://doi.org/10.1175/2010JCLI3277.1.

LeMone, M. A., E. J. Zipser, and S. B. Trier, 1998: The role of environmental shear and thermodynamic conditions in determining the structure and evolution of mesoscale convective systems during TOGA COARE. *J. Atmos. Sci.*, **55**, 3493–3518, https://doi.org/10.1175/1520-0469(1998)055<3493:TROESA>2.0.CO;2.

Lin, Y., and Coauthors, 2012: TWP-ICE global atmospheric model intercomparison: Convection responsiveness and resolution impact. *J. Geophys. Res.*, **117**, D09111, https://doi.org/10.1029/2011JD017018.

Lodoun, T., A. Giannini, P. S. Traore, L. Some, M. Sanon, M. Vaksmann, and J. M. Rsolodimby, 2013: Changes in seasonal descriptors of precipitation in Burkina Faso associated with late 20th century drought and recovery in West Africa. *Environ. Dev.*, **5**, 96–108, https://doi.org/10.1016/j.envdev.2012.11.010.

Lucas, C., E. J. Zipser, and B. S. Ferrier, 2000: Sensitivity of tropical West Pacific Oceanic squall lines to tropospheric wind and moisture profiles. *J. Atmos. Sci.*, **57**, 2351–2373, https://doi.org/10.1175/1520-0469(2000)057<2351:SOTWPO>2.0.CO;2.

Mapes, B. E., 1993: Gregarious tropical convection. *J. Atmos. Sci.*, **50**, 2026–2037, https://doi.org/10.1175/1520-0469(1993)050<2026:GTC>2.0.CO;2.

Marsham, J. H., N. Dixon, L. Garcia-Carreras, G. M. S. Lister, D. J. Parker, P. Knippertz, and C. E. Birch, 2013: The role of moist convection in the West African monsoon system-insights from continental scale convection-permitting simulations. *Geophys. Res. Lett.*, **40**, 1843–1849, https://doi.org/10.1002/grl.50347.

Mathon, V., H. Laurent, and T. Lebel, 2002: Mesoscale convective system rainfall in the Sahel. *J. Appl. Meteor.*, **41**, 1081–1092, https://doi.org/10.1175/1520-0450(2002)041<1081:MCSRIT>2.0.CO;2.

Mohr, K. I., and C. D. Thorncroft, 2006: Intense convective systems in West Africa and their relationship to the African easterly jet. *Quart. J. Roy. Meteor. Soc.*, **132**, 163–176, https://doi.org/10.1256/qj.05.55.

Moncrieff, M. W., 1978: The dynamical structure of two-dimensional steady convection in constant vertical shear. *Quart. J. Roy. Meteor. Soc.*, **104**, 543–567, https://doi.org/10.1002/qj.49710243208.

——, 1981: A theory of organized steady convection and its transport properties. *Quart. J. Roy. Meteor. Soc.*, **107**, 29–50, https://doi.org/10.1002/qj.49710745103.

Newton, C. W., 1960: Morphology of thunderstorms and hailstorms as affected by vertical wind shear. *Physics of Precipitation*, *Geophys. Monogr.*, Vol. 5, Amer. Geophys. Union, 339–346.

Nicholls, M. E., R. H. Johnson, and W. R. Cotton, 1988: The sensitivity of two-dimensional simulations of tropical squall lines to environmental profiles. *J. Atmos. Sci.*, **45**, 3625–3649, https://doi.org/10.1175/1520-0469(1988)045<3625:TSOTDS>2.0.CO;2.

Nicholson, S. E., 2005: On the question of the "recovery" of the rains in the West African Sahel. *J. Arid Environ.*, **63**, 615–641, https://doi.org/10.1016/j.jaridenv.2005.03.004.

Nka, B. N., L. Oudin, H. Karambiri, J. E. Paturel, and P. Ribstein, 2015: Trends in floods in West Africa: Analysis based on 11 catchments in the region. *Hydrol. Earth Syst. Sci.*, **19**, 4707–4719, https://doi.org/10.5194/hess-19-4707-2015.

O'Gorman, P. A., and C. J. Muller, 2010: How closely do changes in surface and column water vapor follow Clausius-Clapeyron

scaling in climate change simulations? *Environ. Res. Lett.*, **5**, 025207, https://doi.org/10.1088/1748-9326/5/2/025207.

Panagos, P., and Coauthors, 2017: Global rainfall erosivity assessment based on high-temporal resolution rainfall records. *Nat. Sci. Rep.*, **7**, 4175, https://doi.org/10.1038/s41598-017-04282-8.

Panthou, G., T. Vischel, and T. Lebel, 2014: Recent trends in the regime of extreme rainfall in the central Sahel. *Int. J. Climatol.*, **34**, 3998–4006, https://doi.org/10.1002/joc.3984.

——, and Coauthors, 2018: Rainfall intensification in tropical semi-arid regions: The Sahelian case. *Environ. Res. Lett.*, **13**, 064013, https://doi.org/10.1088/1748-9326/aac334.

Parker, D. J., 1996: Cold pools in shear. *Quart. J. Roy. Meteor. Soc.*, **122**, 1655–1674, https://doi.org/10.1002/qj.49712253509.

——, and Coauthors, 2005: The diurnal cycle of the West African monsoon circulation. *Quart. J. Roy. Meteor. Soc.*, **131**, 2839–2860, https://doi.org/10.1256/qj.04.52.

Pu, B., and K. H. Cook, 2010: Dynamics of the West African westerly jet. *J. Climate*, **23**, 6263–6276, https://doi.org/10.1175/2010JCLI3648.1.

——, and ——, 2012: Role of the West African westerly jet in Sahel rainfall variations. *J. Climate*, **25**, 2880–2896, https://doi.org/10.1175/JCLI-D-11-00394.1.

Reynolds, R. W., T. M. Smith, C. Liu, D. B. Chelton, K. S. Casey, and M. G. Schlax, 2007: Daily high-resolution-blended analyses for sea surface temperature. *J. Climate*, **20**, 5473–5496, https://doi.org/10.1175/2007JCLI1824.1.

Riede, J. O., R. Posada, A. H. Fink, and F. Kasper, 2016: What's on the 5th IPCC report for West Africa? *Adaption to Climate Change and Variability in Rural West Africa*, J. A. Yaro and J. Hesselberg, Eds., Springer, 7–24.

Rotunno, R., J. B. Klemp, and M. L. Weisman, 1988: A theory for strong, long-lived squall lines. *J. Atmos. Sci.*, **45**, 463–485, https://doi.org/10.1175/1520-0469(1988)045<0463:ATFSLL>2.0.CO;2.

Sanogo, S., A. H. Fink, J. A. Omotosho, A. Ba, R. Redl, and V. Ermert, 2015: Spatio-temporal characteristics of the recent rainfall recovery in West Africa. *J. Climatol.*, **35**, 4589–4605, https://doi.org/10.1002/joc.4309.

Smith, R. N. B., 1990: A scheme for predicting layer clouds and their water content in a general circulation model. *Quart. J. Roy. Meteor. Soc.*, **116**, 435–460, https://doi.org/10.1002/qj.49711649210.

Stein, T. H. M., D. J. Parker, R. J. Hogan, C. E. Birch, C. E. Holloway, G. M. S. Lister, J. H. Marsham, and S. J. Woolnough, 2015: The representation of the West African monsoon vertical cloud structure in the Met Office unified model: An evaluation with CloudSat. *Quart. J. Roy. Meteor. Soc.*, **141**, 3312–3324, https://doi.org/10.1002/qj.2614.

Stratton, R. A., and Coauthors, 2018: A Pan-African convection-permitting regional climate simulation with the Met Office Unified Model: CP4-Africa. *J. Climate*, **31**, 3485–3508, https://doi.org/10.1175/JCLI-D-17-0503.1.

Takemi, T., 2007: A sensitivity of squall line intensity to environmental static stability under various shear and moisture conditions. *Atmos. Res.*, **84**, 374–389, https://doi.org/10.1016/j.atmosres.2006.10.001.

——, 2010: Dependence of the precipitation intensity in mesoscale convective systems to temperature lapse rate. *Atmos. Res.*, **96**, 273–285, https://doi.org/10.1016/j.atmosres.2009.09.002.

——, 2012: Projected regional-scale changes in atmospheric stability condition for the development of summertime convective precipitation in the Tokyo metropolitan area under global warming. *Hydrol. Res. Lett.*, **6**, 17–22, https://doi.org/10.3178/hrl.6.17.

——, 2014: Convection and precipitation under various stability and shear conditions: Squall lines in tropical versus midlatitude environment. *Atmos. Res.*, **142**, 111–123, https://doi.org/10.1016/j.atmosres.2013.07.010.

——, S. Nomura, Y. Oku, and H. Ishikawa, 2012: A regional-scale evaluation of changes in environmental stability for summertime afternoon precipitation under global warming from super-high-resolution GCM simulations: A study for the case in the Kanto plain. *J. Meteor. Soc. Japan*, **90A**, 189–212, https://doi.org/10.2151/jmsj.2012-A10.

Tao, W.-K., J. R. Scala, B. S. Ferrier, and J. Simpson, 1995: The effect of melting processes on the development of a tropical and a midlatitude squall line. *J. Atmos. Sci.*, **52**, 1934–1948, https://doi.org/10.1175/1520-0469(1995)052%3C1934:TEOMPO%3E2.0.CO;2.

Taylor, C. M., and Coauthors, 2017: Frequency of extreme Sahelian storms tripled since 1982 in satellite observations. *Nature*, **544**, 475–478, https://doi.org/10.1038/nature22069.

Tazan, F., A. Diarra, R. F. W. Kabore, B. Ibrahim, M. Bologo Traore, K. Traore, and H. Karambiri, 2019: Trends in flood events and their relationship to extreme rainfall in an urban area of Sahelian West Africa: The case study of Ouagadougou, Burkina Faso. *J. Flood Risk Manage.*, **12**, e12507, https://doi.org/10.1111/JFR3.12507.

Thorpe, A. J., M. J. Miller, and M. W. Moncrieff, 1982: Two-dimensional convection in nonconstant shear: A model of mid-latitude squall lines. *Quart. J. Roy. Meteor. Soc.*, **108**, 739–762, https://doi.org/10.1002/qj.49710845802.

USAID, 2017: Climate change risk profile: West Africa Sahel. USAID, 10 pp., https://www.climatelinks.org/resources/climate-change-risk-profile-west-africa-sahel.

Vellinga, M., M. Roberts, P. L. Vidale, M. S. Mizielinski, M.-E. Demory, R. Schiemann, J. Strachan, and C. Bain, 2016: Sahel decadal rainfall variability and the role of model horizontal resolution. *Geophys. Res. Lett.*, **43**, 326–333, https://doi.org/10.1002/2015GL066690.

Vizy, E. K., and K. H. Cook, 2017: Seasonality of the observed amplified Sahara warming trend and implications for Sahel rainfall. *J. Climate*, **30**, 3073–3094, https://doi.org/10.1175/JCLI-D-16-0687.1.

——, and ——, 2018: Mesoscale convective systems and nocturnal rainfall over the West African Sahel: Role of the inter-tropical front. *Climate Dyn.*, **50**, 587–614, https://doi.org/10.1007/s00382-017-3628-7.

——, and ——, 2019: Understanding the summertime diurnal cycle of precipitation over sub-Saharan West Africa: Regions with daytime rainfall peaks in the absence of significant topographic features. *Climate Dyn.*, **52**, 2903–2922, https://doi.org/10.1007/S00382-018-4315-Z.

——, ——, J. Cretat, and N. Neupane, 2013: Projections of a wetter Sahel in the twenty-first century from global and regional models. *J. Climate*, **26**, 4664–4687, https://doi.org/10.1175/JCLI-D-12-00533.1.

Walters, D., and Coauthors, 2019: The Met Office unified model global atmosphere 7.0/7.1 and JULES global land 7.0 configurations. *Geosci. Model Dev.*, **12**, 1909–1963, https://doi.org/10.5194/gmd-12-1909-2019.

Wilcox, C., and Coauthors, 2018: Trends in hydrological extremes in the Senegal and Niger Rivers. *J. Hydrol.*, **566**, 531–545, https://doi.org/10.1016/j.jhydrol.2018.07.063.

Wood, N., and Coauthors, 2014: An inherently mass-conserving semi-implicit semi-Lagrangian discretization of the deep-atmosphere global non-hydrostatic equations. *Quart. J. Roy. Meteor. Soc.*, **140**, 1505–1520, https://doi.org/10.1002/qj.2235.